Paper #5036 – Revision 1

Bubbles matter: An assessment of the contribution of vapor bubbles to melt inclusion volatile budgets

Lowell Moore[1], Esteban Gazel[1], Robin Tuohy[2], Alex Lloyd[3], Rosario Esposito[4], Matthew Steele-MacInnis[5], Erik H. Hauri[6], Paul J. Wallace[2], Terry Plank[3], Robert J. Bodnar[1,7]

[1] Department of Geosciences, Virginia Tech, Blacksburg, VA, USA 24061

[2] Department of Geological Sciences, University of Oregon, Eugene, OR, USA 97403

[3] Lamont-Doherty Earth Observatory, Columbia University, Palisades, NY, USA 10964

[4] Dipartimento di Scienze della Terra, dell'Ambiente e delle Risorse, Università di Napoli Federico II, Napoli, Italy

[5] Institute for Geochemistry and Petrology, ETH, 8092 Zurich, Switzerland

[6] Department of Terrestrial Magnetism, Carnegie Institute of Washington, Washington DC, USA 20015

[7] Corresponding Author

ABSTRACT

Melt inclusions (MI) are considered the best tool available for determining the pre-eruptive volatile contents of magmas. H_2O and CO_2 concentrations of the glass phase in MI are commonly used both as a barometer and to track magma degassing behavior during ascent due to the strong pressure dependence of H_2O and CO_2 solubilities in silicate melts. The often unstated and sometimes overlooked requirement for this method to be valid is that the glass phase in the MI must represent the composition of the melt that was trapped at depth in the volcanic plumbing system. However, melt inclusions commonly contain a vapor bubble that formed after trapping owing to differential shrinkage of the melt compared to the host crystal, and/or crystallization at the inclusion-host interface. Such bubbles may contain a substantial portion of volatiles, such as CO_2, that were originally dissolved in the melt. In this study, we determined the contribution of CO_2 in the vapor bubble to the overall CO_2 content of MI based on quantitative Raman analysis of the vapor bubbles in MI from the 1959 Kilauea Iki (Hawaii), 1960 Kapoho (Hawaii), 1974 Fuego volcano (Guatemala), and 1977 Seguam Island (Alaska) eruptions. We found that the bubbles typically contain 40 to 90% of the total CO_2 in the MI. Reconstructing the original CO_2 content by adding the CO_2 in the bubble back into the melt results in an increase in CO_2 concentration by as much as an order of magnitude (1000s of ppm). Reconstructed CO_2 concentrations correspond to trapping pressures that are significantly greater than one would predict based on analysis of the volatiles in the glass alone. Trapping depths can be as much as 10 km deeper than estimates that ignore the CO_2 in the bubble. In addition to CO_2 in the vapor bubbles, many MI showed the presence of a carbonate mineral phase. Failure to recognize the carbonate during petrographic examination or analysis of the glass and to include its contained CO_2 when reconstructing the CO_2 content of the originally trapped melt will introduce additional errors into the calculated volatile budget. Our results emphasize that accurate determination of the pre-eruptive volatile content of melts based on analysis of melt inclusions must consider the volatiles contained in the bubble (and carbonates, if present). This can be accomplished either by analysis of the bubble and the glass followed by mass-balance reconstruction of the original volatile content of the melt, or by re-homogenization of the MI prior to conducting microanalysis of the quenched, glassy MI.

Keywords: melt inclusion; degassing path; Raman spectroscopy; carbon dioxide; vapor bubble

INTRODUCTION

It is well known that volatile contents and magma degassing behavior affect the style, frequency, and intensity of near-surface magmatic and volcanic processes (Sparks, 1978; Burnham and Ohmoto, 1980; Webster et al., 2001; Métrich and Wallace, 2008; and references therein). For this reason, much effort has been devoted to characterizing the volatile evolution of shallow magmatic (volcanic) systems to better constrain volcanic history. Unfortunately, bulk rock or volcanic glass samples rarely reflect the pre-eruptive volatile content of a melt because the volatiles are lost from the system as the pressure decreases (Stolper & Holloway, 1988; Dixon et al., 1995) when magma approaches the surface and erupts.

Melt inclusions (MI) are droplets of melt trapped as defects in a growing crystal, often as a result of varying crystal growth rates (Roedder, 1979; 1984; Métrich and Wallace, 2008). MI can occur in isolation, or in assemblages (MIA) that are randomly scattered or organized along growth zones within the host crystal. MI represent samples of melt that were isolated from the bulk magma at depth, thus preserving the composition of the pre-eruptive material (Roedder, 1979). For this reason, MI are particularly useful for determining pre-eruptive volatile budgets of volcanic systems, and MI are now routinely used to study a wide variety of volcanic and intrusive igneous processes (Roedder, 1979; Anderson et al., 2000; Hauri et al., 2002; Lowenstern, 2003; Wallace, 2005; Bodnar and Student, 2006; Gazel et al., 2012, Audétat and Lowenstern, 2014).

The analysis and interpretation of MI can be challenging because MI may experience post-entrapment modifications between the time of trapping, later eruption onto the surface, and analysis in the laboratory (Roedder, 1979; 1984). In particular, diffusion of H^+ through the host, resulting in loss of H_2O (Hauri, 2002; Massare et al., 2002; Severs et al., 2007; Gaetani et al, 2012; Bucholz et al., 2013), and post-entrapment crystallization (PEC) (Danyushevsky et al., 2002; Steele-MacInnis et al., 2011) can affect the composition of the melt (glass) in the MI. These combined effects can produce trends in the H_2O-CO_2 content of the glass phase that are similar to those produced as a result of magma degassing (Gaetani et al., 2012; Steele-MacInnis et al., 2011; Bucholz et al., 2013).

The formation of a bubble in a MI after trapping is a natural consequence of the PVTX properties of crystal-melt-volatile systems (Lowenstern, 1995). Following entrapment, as the host phenocryst and its contained MI cool, the volume occupied by the melt will decrease more (a larger percentage) than that of the host phenocryst owing to their different thermal expansion properties, i.e., silicate liquids shrink more than their host crystals during cooling. Further reduction in the melt (glass) volume is associated with PEC because the molar volume of the mineral (olivine for example) that precipitates on the MI wall is less than the partial molar volume of that component (i.e., the "olivine" component) in the melt phase. If melts do not remain metastable or "stretched" (Lowenstern, 1995) during initial cooling, a void (bubble) forms in the MI as a necessary consequence of these processes (Roedder, 1979; 1984). If the melt is volatile-free, the void (bubble) would be a vacuum (ignoring the very low vapor pressure of volatile-free silicate melts and glass). However, if the melt contains volatiles such as H_2O or CO_2 that become less soluble with decreasing pressure (Dixon et al., 1995), the decrease in pressure associated with melt contraction would necessarily lead to the exsolution of some of the volatile component from the melt and into the vapor bubble. Thus, formation of a vapor bubble could deplete the melt in some, or most, of its volatiles.

Previous workers have recognized that bubble formation is an obstacle which affects the interpretation of MI trapping conditions based only on analysis of the glass phase. Approaches to address and/or correct for the presence of bubbles in MI vary. Some workers have avoided or limited the inclusion of bubble-bearing MI in their study (Lowenstern, 1994a; Wallace and Gerlach, 1994; Wallace et al., 1999; Rapien et al., 2003; Helo et al., 2011; Esposito et al., 2011; Lloyd et al., 2013). When only bubble-bearing MI were available for study, some workers have acknowledged potential contributions from the bubble by stating that the CO_2 contents and pressures determined from the MI are minimum values (Anderson and Brown, 1993; Cervantes and Wallace, 2003; Spilliaert et al., 2006; Kamenetsky et al., 2007; Johnson et al., 2008; Vigouroux et al., 2008; Ruscitto et al., 2010; Esposito et al., 2011). Some have attempted to homogenize and quench bubble-bearing MI to eliminate the bubble and produce a homogeneous glass before analysis (Skirius et al., 1990; Yang and Bodnar, 1994; Cervantes et al., 2002; Student and Bodnar, 2004; Tuohy, 2013; Tuohy et al., in prep.). Others report that bubbles are present, but do not further discuss their potential contribution to MI volatile abundances (Lowenstern, 1994a; Roggensack et al., 1997; Walker, 2003; Liu et al., 2006; Mangiacapra et al., 2008; Lloyd et al., 2013). Schipper et al. (2010) argue that, based on a positive correlation between CO_2, H_2O, and MgO in their high-Fe MI, the bubbles in these MI were likely either trapped heterogeneously or only contain a vacuum and should be ignored in either case. We note, however, that it is not possible for a volatile-bearing MI to contain a shrinkage bubble that contains no mass (i.e., contains none of the volatiles that were originally dissolved in the melt). For this to occur, at the moment that the shrinkage bubble forms in the MI, the pressure in the shrinkage bubble would be a vacuum (~0 MPa) while the immediately adjacent melt would be at some much higher pressure, and this pressure “gradient” or “discontinuity” would have to be maintained during continued cooling - an impossible scenario. Thus, any bubble contained in a volatile-bearing MI must also contain some volatiles.

Pseudo degassing paths

Before discussing our results, it is instructive to note that it is possible to trap a suite of MI with uniform volatile contents and generate a range in volatile contents in the glass phase through mass transfer of volatiles from the melt to the bubble after trapping. To demonstrate this principle, we have calculated the trend in H_2O-CO_2 contents that would be generated if a suite of inclusions are all trapped at the same temperature and pressure, and all trap a melt containing 1200 ppm CO_2. Then, following trapping, vapor bubbles having various sizes (0.5 to 2.0 volume percent of the MI) and CO_2 densities (0.04 to 0.16 g/cm^3) form in the MI. Variable bubble size and fluid density might be expected if a group of MI that were all trapped at the same time exsolve various proportions of the dissolved volatiles into the bubble before reaching the glass transition temperature (T glass). As the MI cools and becomes volatile-saturated, the volatiles must diffuse through the melt and into the bubble. If the rate of cooling is too fast, exsolving volatiles may not be able to diffuse towards the bubble sufficiently fast to maintain equilibrium between the melt and bubble before the glass transition temperature is reached. Thus, cooling rates of MI vary as a function of the clast and/or phenocryst grain size, depth of burial in the eruptive sequence, etc., and MI from tephras are expected to cool more quickly than those from lavas or intrusive bodies (Lloyd et al., 2013). Under these conditions, we might expect that inclusions with different sizes and in different crystals might show a range of bubble sizes and fluid densities in the bubbles.

The trend that might be produced from the suite of MI described above that all contain the same total amount of CO_2 is shown in Figure 1. This trend is similar to trends produced as a result of open-system degassing (e.g., Lowenstern, 1994a; Walker, 2003). If the CO_2 contained in the bubbles in this scenario were then "added back into" the melt, the reconstructed CO_2 concentration would be the same for every inclusion (i.e., 1200 ppm). Note that we assume that the concentration of H_2O in the melt remains constant (Figure 1, symbols are slightly offset so they can be viewed easily). This assumption is appropriate for melts with low H_2O contents such as those trapped in MI from Kilauea. Low H_2O contents in vapor bubbles are also reported for MI from the Marianas Arc by Shaw et al. (2008) (calculated based on the H_2O and CO_2 contents of the glass, using the ideal gas law to estimate the number of moles of H_2O and CO_2 in the bubble), and by Wallace et al. (in review) for MI in Mauna Loa picrite (based on comparison of H_2O contents of glass in naturally quenched MI with that of glass in experimentally rehomogenized MI). However, for melts that contain higher concentrations of H_2O (like those from Fuego or Seguam), a significant portion of the H_2O in the melt might exsolve from the melt if pressure in the MI were to drop to less than about 1000 bars, thus changing the H_2O content of the remaining melt (glass). We emphasize that the trend shown in Figure 1 is similar to that which has been reported from many volcanic systems and interpreted to represent a degassing path. We are not suggesting that all such degassing trends are spurious, but the trend in Figure 1 highlights the importance of including the amount of CO_2 contained in the bubble when estimating the volatile content of the trapped melt.

Quantifying the amount of CO_2 contained in vapor bubbles in MI

Some workers have recognized that vapor bubbles could contain some portion of the volatiles that were originally dissolved in the melt, and have attempted to quantify the contribution of the vapor bubble to the total volatile budget. For example, Anderson and Brown (1993) estimated the amount of CO_2 contained in the vapor bubbles of a suite of MI from

Kilauea by estimating the change in volume of the bubble associated with changes in temperature and pressure during cooling. Cervantes et al. (2002) homogenized MI from a Mauna Loa picrite and found that ~80% of the CO_2 in the MI had been lost to the bubble during post-entrapment cooling (Wallace et al, in review). Shaw et al. (2008) obtained a similar result for a suite of Mariana Arc MI by measuring the H_2O and CO_2 concentrations in the glass and then using the Ideal Gas Law (IGL) to calculate the amount of CO_2 in the bubble (see below). Esposito et al. (2011) measured the density of CO_2 in a vapor bubble in a MI from the Solchiaro eruption at Procida Island, Italy, using Raman spectroscopy, and determined the concentration of CO_2 in the glass using secondary ion mass spectrometry (SIMS). Mass balance reconstruction (using a method described by Esposito et al., 2011) of the bulk composition of the trapped melt revealed that the vapor bubble contained ~64% of the total CO_2 in the MI. Using a similar approach, Hartley et al. (2014) reconstructed the compositions of a suite of MI from the 1783-1784 Laki eruption in Iceland and found that >90 percent of the CO_2 in the MI can be contained in the bubble.

Raman analysis provides a fast, simple, and non-destructive method to determine the density of CO_2. Kawakami et al. (2003) found that the density of CO_2 is related to the distance between two Raman lines (collectively referred to as the Fermi diad) (Figure 2). Fall et al. (2011) extended and modified the densimeter and applied it to determine salinities of CO_2-bearing fluid inclusions based on the clathrate melting temperatures and pressures estimated from the CO_2 density. We note that it is also possible to detect H_2O using Raman spectroscopy, but determining the amount of H_2O in the vapor phase using this method is difficult because, unlike CO_2, H_2O appears in the Raman spectrum of both the glass and vapor phases (i.e. we are not yet able to distinguish the source of the 3500 cm^{-1} O-H band when analyzing a bubble that is surrounded by glass that also contains H_2O).

In this study, we analyzed bubble-bearing MI from various locations to determine the CO_2 concentration in the trapped melt by adding the amount of CO_2 in the bubble to the amount contained in the glass. We analyzed vapor bubbles in melt inclusions in olivine phenocrysts from Fuego volcano, Guatemala (1974 eruption), from Seguam Island, Alaska (1977 eruption), and from the summit and East Rift Zone of Kilauea, Hawaii (the 1959 Kilauea Iki and 1960 Kapoho eruptions, respectively). We used a combination of SIMS and Fourier transform infrared spectroscopy (FTIR; Tuohy et al., in preparation) to determine the volatile content of the glass, and we used Raman spectroscopy to quantify the density of CO_2 in the vapor phase. We then used a mass balance method (Esposito et al., 2011) to reconstruct the total CO_2 concentrations of MI and evaluate the contribution of the bubble to the MI volatile budget. Finally, we consider implications of our results for predicting magma degassing behavior in volcanic systems.

METHODS

Sample collection and preparation

The MI analyzed in this study were contained in tephras that have been studied previously (listed below). We did not analyze the same inclusions as were analyzed in the earlier studies, but the MI analyzed in this study were contained in olivines that were separated from the same bulk tephra samples that were used previously. The tephras come from Kilauea (Hawaii), Fuego volcano (Guatemala), and Seguam Island (Alaska). A summary of the various methods used in this and previous studies to analyze the MI is given in Table 1.

The tephras from Kilauea were erupted during the 1959 Kilauea Iki and 1960 Kapoho eruptions described by Richter et al. (1970). MI in olivines from Kilauea Iki tephra (Fo 84-88) were previously described and analyzed by Anderson and Brown (1993), who calculated trapping pressures (mostly ≤1 kbar) using volatile contents measured from the glass and discussed the significance of CO_2 contained in bubbles. The samples from Kilauea Iki and Kapoho analyzed in this study (Samples Kil Iki Nat R, and Kap 8 Nat R) were collected by R. Tuohy and D. Swanson (Tuohy, 2013; Tuohy et al., in preparation).

Olivine phenocrysts from Fuego volcano were isolated from a population of tephra samples collected during the October 1974 eruption by Rose et al. (1978). MI from these samples were prepared and analyzed by Lloyd et al. (2013), who found that sample clast size affects the temperature-controlled H^+ diffusion through olivine. The MI from Fuego analyzed in this study were from the same suite of olivine phenocrysts that were separated by Lloyd et al. (2013) (sample VF-74-131).

Tephras from Seguam Island were erupted during the 1977 Pyre Peak eruption (Jicha et al., 2006). The samples were collected and olivine separates were prepared as described by Zimmer et al. (2010), who measured water contents of MI to investigate the role of water in generation of the calc-alkaline trend. The olivine separates from Seguam described in this study were prepared by Zimmer et al. (2010) (sample SEG07-06).

The olivine phenocrysts from Kilauea were mounted individually on glass slides using Crystalbond™ and polished. Olivine phenocrysts from both Fuego and Seguam were also mounted individually by attaching each crystal to the end of a 2.5 mm diameter glass rod using Crystalbond™ and polished following the methodology described by Thomas & Bodnar (2002). Crystals were polished on an abrasive pad (3 μm diamond suspension) until the target MI was sufficiently close to the surface of the crystal for Raman analysis (~a few microns below the surface) and then final polishing was completed with a 0.3 μm alumina suspension. Individual crystals were mounted and polished to allow greater control over the amount of host material surrounding the MI that was removed during polishing to assure that none of the vapor bubbles would be breached during sample preparation, while at the same time allowing enough material to be removed to bring the target MI close to the crystal surface.

The MI from Kilauea Iki and Kapoho (Figure 3a,b) are generally smooth-walled, clear, and round to subhedral (negative crystal shape). About eighty percent of the MI contain a vapor bubble that occupies between ~1 and 10 volume percent of the inclusion (Table 2). Some of the MI also contain a small (≤1 volume percent) opaque daughter crystal of chromite, and a few of the inclusions contain larger (10's of volume percent) chromite crystals that were likely co-trapped with the melt. The olivine host also contains many chromite inclusions, as well as clusters of chromite with small amounts of interstitial melt. Chromite is a common phase in olivine-hosted MI from Kilauea (e.g., Anderson and Brown, 1993), and chromite was likely growing at the same time as the olivine phenocrysts.

The MI from Fuego volcano are round to euhedral (negative crystal shape), with walls that have a smooth to wrinkled texture (Fig 3c). Most of the MI contain a single vapor bubble. The vapor bubbles range from ~1 - 5 volume percent of the MI (Table 3). Some of the MI also contain blocky, opaque crystals that occupy ~3 volume percent of the MI (Fig. 3c), and some of these have filiform microcrysts radiating from them. Although not all of the MI contain the opaque phase, the volume proportion of the MI occupied by the phase is relatively consistent in those that do contain the opaque mineral. As such, we interpret the opaque phase to be a daughter mineral that was precipitated from the melt after trapping. These daughter minerals could have grown rapidly due to undercooling of the MI (Roedder, 1979), and if the crystals represent volatile-free phases the melt (glass) would be enriched in volatiles (relative to the melt that was originally trapped in the MI) as a result of this post-entrapment crystallization.

The MI from Seguam (Fig. 3d) are more uniform in color and texture compared to those from Kilauea and Fuego. The inclusions are all essentially clear, tan, and bubble-bearing. All of the larger (> ~50 μm) inclusions have a wrinkled texture. The bubbles occupy between <1 and 6 volume percent of the MI.

MI from all three sample suites were examined on a petrographic microscope and photographed. The images were analyzed using image analysis software (ImageJ and LabSpec) to determine the dimensions of MI and vapor bubbles. Most of the MI were oblate in shape and the long and short axes were measured and the volume was approximated as an oblate spheroid. The vapor bubbles were approximately circular (long axis ≈ short axis) when examined under the microscope and the volumes could thus be estimated by assuming a spherical geometry. Where the bubbles were slightly oblate, we used the average diameter to calculate the volume.We also evaluated the distribution of vapor bubble dimensions within a population of MI from each sample suite or within individual olivine grains to distinguish between MI that trapped bubbles along with the melt, and those that trapped only melt and nucleated a vapor bubble in the MI after trapping. Each phenocryst from Kilauea contained multiple MI, allowing us to evaluate the volume percent vapor for MI in each phenocryst individually as shown in Figure 4a. Individual phenocrysts from Fuego and Seguam generally host fewer MI. The MI in these samples do not contain anomalously large (>10 volume percent) vapor bubbles that might suggest either heterogeneous trapping or reequilibration. For this reason, the volumetric properties for all Fuego MI and for all Seguam MI are combined in Figure 4b.

Raman, SIMS, FTIR and EPMA analysis

Raman spectra were collected using a JY Horiba LabRam HR (800 mm) Raman spectrometer equipped with a 100 mW 514 nm argon laser, confocal hole diameter of 400 μm, 600 mm^{-1} and 1800 mm^{-1} gratings, and slit width of 150 μm. Three 30-s scans were collected and averaged. GRAMS/AI and LabSpec software were used to apply a baseline correction to each spectrum and to fit the CO_2 peaks using a mixed Gaussian/Lorentzian method. During every analytical session, the CO_2 bubble in a synthetic H_2O-CO_2 fluid inclusion (Sterner & Bodnar, 1984) was analyzed to test for reproducibility in determination the splitting of the Fermi diad.

Following peak fitting, the distance between the two peaks of the Fermi diad (peak splitting) was determined and the density was calculated from the peak splitting using the equation of Fall et al. (2011). While CO_2 was detected in a large number of the vapor bubbles, as evidenced by the presence of the Fermi diad, the density of the CO_2 could not be quantified for all cases where the Fermi diad was observed. In some cases, the Fermi diad splitting (Δ, cm^{-1}) was outside of the range over which the equation of Fall et al. (2011) is valid – usually this applied to bubbles with very low CO_2 density. In other cases, the spectra were of poor quality with low peak intensities, and thus did not allow precise determination of peak positions and calculation of the Fermi diad splitting. For these inclusions, we noted that CO_2 was detected but the density could not be quantified. Finally, it should be emphasized that failure to identify CO_2 in a given MI during Raman analysis does not necessarily mean that CO_2 is not present. The ability to detect a given species by Raman is a function of many factors, including but not limited to concentration (or number of moles) of the species in the analytical volume, depth of the analytical volume beneath the mineral surface, shape of the MI-host interface (which affects light transmission), fluorescence from the host and/or glues used to mount the sample, etc. (Burke, 1994; Burruss, 2003; Frezzotti, 2012).

Following Raman analysis, samples were prepared for analysis of the glass in the MI. A subset of MI from Kilauea was analyzed by FTIR at the University of Oregon (Tuohy et al., in preparation), and a subset of MI from Seguam and Fuego was analyzed by SIMS at the Carnegie Institution of Washington (CIW). To prepare for SIMS analysis, the olivine phenocrysts were polished further (using the same method described above) until the glassy part of the target MI was exposed at the surface. After polishing, the fiberglass rod mounts were immersed in a series of acetone baths, each for a period of one minute, to completely dissolve the Crystalbond™ adhesive. The olivine phenocrysts were then pressed individually into a one-inch round indium mount in preparation for SIMS analysis.

Volatile contents of the MI glass were determined using a Cameca 6f secondary ion mass spectrometer (SIMS) at the Department of Terrestrial Magnetism, Carnegie Institution of Washington. The ion beam was rastered over a 25 μm-wide spot using a 10-15 nA, 10 kV Cs+ ion beam; a 10 μm aperture was used to restrict the analytical area to a 10 μm spot. The reader is referred to Hauri et al. (2002) for a more detailed description for the analytical method . Analytical errors for all SIMS analyses of CO_2 and H_2O are less than 10% and 2%, respectively. Reported errors represent reproducibility of the analyses on homogeneous basaltic standard glasses; errors on standard calibrations are 1-2%.

Following SIMS analysis, major elements were measured by electron probe microanalysis (EPMA) at Virginia Tech to obtain major element data that could be used to estimate the amount of PEC in the MI. The major element compositions of the MI glass and olivine host phenocrysts were measured using a Cameca SX-50 Electron Probe Microanalyzer.

The glass and olivine host were analyzed with a 1 µm beam and 15 kV accelerating voltage. The olivine host was analyzed using a 21.9 nA current, and the glasses were analyzed with a 9.9 nA current. When major element compositions + H_2O did not sum to 100±1 weight percent, the major element data was not used. We used a lower current to analyze MI glass than to analyze the olivine host to minimize Na loss from the glass. It is still possible that some Na was lost, and this would result in a slight overestimate of other major element abundances used to calculate the effect of PEC on the MI volatile contents. However, Na loss should have a negligible effect on our conclusions because (as described below) the amount of PEC experienced by the MI is minor.

Major element and volatile contents of the MI glass were corrected for PEC and Fe loss using Petrolog3 software (Danyushevsky & Plechov, 2011). MI from Kilauea were corrected by Tuohy et al. (in preparation), also using Petrolog3. PEC corrections for Fuego and Seguam were calculated using the Lange & Carmichael (1987) model for melt density, the Ford et al. (1983) olivine-melt model, the Borisov & Shapkin (1990) model for melt oxidation state, assuming that oxygen fugacity is buffered at Ni-NiO. We used the Ni-NiO buffer because Zimmer et al. (2010) and Lloyd et al. (2013) have shown that melts from Seguam and Fuego consistently have oxygen fugacities 0-2 log units above the Fayalite-Magnetite-Quartz (FMQ) buffer. We also modeled PEC corrections assuming that oxygen fugacity is buffered at FMQ and the results were nearly identical – most likely because the amount of PEC experienced by the MI was so small (see below).

The concentration of CO_2 in the melt that was originally trapped in the MI was estimated by combining the FTIR (Tuohy et al., in preparation) and SIMS data with the Raman data and applying the mass balance method described in Esposito et al. (2011). For the MI from Kilauea that were too small and too numerous in individual phenocrysts to analyze by FTIR, we assumed that the glass contained no CO_2 when estimating the bulk (total) CO_2 in the MI. This results in a minimum value for the amount of CO_2 in the melt that was originally trapped in the MI and is a reliable estimate of the total CO_2 content for those MI in which most of the CO_2 is in the bubble. Details of Raman, SIMS, EPMA, mass balance reconstructions, and PEC corrections are described in the supplementary materials.

RESULTS and DISCUSSION

Raman analyses

Vapor bubbles in 148 MI from the Kilauea Iki and Kapoho (Hawaii) eruptions were analyzed by Raman, including 75 MI from the Kilauea Iki eruption and 73 MI from the Kapoho eruption. CO_2 was detected in 111 of the bubbles analyzed (i.e., the Fermi diad is clearly distinguishable), and the CO_2 density could be quantified with reasonable precision in 98 of the bubbles analyzed. The density of CO_2 in vapor bubbles in MI from both Kilauea Iki and Kapoho ranges from <0.01 to 0.29 g/cm^3. During Raman analysis, carbonate minerals were also detected (as evidenced by a peak at 1090 cm^{-1} in the Raman spectra) in four of the fifteen bubble-bearing MI from a phenocryst associated with the Kapoho eruption (sample Kap 8 Nat R 2). These carbonate phases could represent the product of reaction between CO_2 that exsolved from the melt after trapping and the still hot melt or glass in the MI (Andersen et al., 1984).

Raman spectra were obtained from bubbles in 35 MI from Fuego. CO_2 was detected in 12 of the bubbles and could be quantified in 10 of the bubbles. The density of CO_2 in the bubbles ranges from 0.07 to 0.26 g/cm^3. Carbonates were also detected during analysis of 16 of the 35 vapor bubbles (Table 3).

Raman spectra were collected from 48 bubbles in MI from Seguam. We detected CO_2 in 19 of these bubbles, and the density could be quantified with reasonable precision in 13 bubbles. The CO_2 densities range from 0.01 to 0.07 g/cm^3. No daughter minerals (or co-trapped) phases were observed in MI from Seguam, with the exception of carbonates at the bubble-glass interface (Table 4). Figures 3e, f show a texture that we associate with the presence of carbonates. This texture is commonly visible when viewing bubbles in MI from Seguam in reflected light. During Raman analysis of the bubble shown in Figure 3e, carbonates were not detected until the analytical spot was positioned over the bright spot shown near the center of Figure 3f. In Table 4, we record the petrographic evidence for the carbonate mineral and the presence of a carbonate peak in the Raman spectra separately, but we consider either to indicate the presence of carbonates.

Volumetric analysis of MI

Before conducting mass-balance calculations to quantify the amount of CO_2 contained in the bubble, it is first necessary to confirm that the CO_2 in the vapor bubbles was originally dissolved in the melt and subsequently exsolved from the melt after trapping. If MI trapped various proportions of melt and vapor, we would expect a wide range in the relative size of the vapor bubbles in MI, whereas if the vapor bubbles exsolved from the melt after trapping we would expect to see a relatively uniform vapor bubble to glass volume ratio in the MI. To assess whether the vapor bubbles in MI were trapped along with melt, or were generated after trapping by volatile exsolution from the melt, the bubble and MI volumes were estimated as described above (see methods). The relationship between MI and vapor bubble size of two Kilauea Iki samples is shown for two phenocrysts in Figure 4a. Most inclusions in phenocryst Kil Iki Nat R

6 exhibit a linear relationship between MI volume and bubble volume. This indicates a constant volume proportion vapor in the MI and suggests that the vapor bubbles represent volatiles that were originally dissolved in the melt at the time of trapping and later exsolved from the melt after it was isolated as a melt inclusion. However, several of the MI in phenocryst Kil Iki Nat R 4 contain vapor bubbles that vary in volume over two orders of magnitude and show no correlation with MI volume (i.e., the volume proportion of the MI occupied by the vapor bubble is not constant). These MI were grouped together in a single melt inclusion assemblage (MIA) and are the only group identified in this study that show significant variation in bubble volume. We interpret this MIA to have trapped inclusions with various proportions of vapor and melt. Although it appears that only the smaller MI ($<10^3$ μm^3) trapped vapor as a separate phase, and all of these were in the same MIA, we exclude all of the MI hosted by phenocryst Kil Iki Nat R 4 from further discussion as a precaution. Similar to the majority of the Kilauea MI, the vapor bubble volumes versus MI volumes for Fuego and Seguam MI display a linear relationship (~3 volume percent) that suggests that the vapor bubbles were exsolved from the melt after trapping. Therefore, the volatile content of the MI from Fuego and Seguam (glass + bubble) are representative of the volatile content of the melt at the time of trapping.

Reconstructing the original CO_2 content of the trapped melt

Using the density of CO_2 in the vapor bubbles in MI obtained from Raman analysis, combined with the volumetric proportions of vapor bubble and glass in the MI, the CO_2 content of the trapped melt can be reconstructed using a mass balance approach (Esposito et al., 2011; Esposito et al., 2011). We consider two cases: one case in which the CO_2 content of the glass is not known, and one case in which the CO_2 content of the glass is known from SIMS and/or FTIR analysis. In the first case where the CO_2 content of the glass is not known, we consider two variations – one in which the CO_2 content of the glass can be approximated based on previous studies of MI from the same eruptive unit, and a second in which no data are available to constrain the CO_2 content of the glass. After reconstructing the CO_2 content of the trapped melt we discuss the proportion of the total CO_2 in the MI that is contained in the vapor bubble, and implications for estimating depths of formation and degassing paths if the CO_2 in the vapor bubble is ignored.

The CO_2 content of the glass in the MI is unknown. In some studies, it may be possible to determine the CO_2 density in the vapor bubble and the volumetric proportions of vapor and glass in the MI, but the volatile content of the glass phase is unknown. For example, while vapor bubbles as small as about 1-2 µm in diameter can be analyzed by Raman, if the glass phase in MI is less than about 20 µm in minimum dimension it generally can not be analyzed by conventional SIMS or FTIR. For such MI, it is possible to estimate a minimum CO_2 content of the trapped melt using results from Raman spectroscopy only. This is particularly useful because most of the MI from Kilauea examined in this study were too small and too numerous to be analyzed by FTIR or SIMS and, thus, the CO_2 content of the glass phase in these MI is unknown. If we assume that the glass contains 0 ppm CO_2, a minimum CO_2 content for the MI is obtained by simply adding the CO_2 in the bubble into the glass, using the relative volume proportions of bubble and glass determined previously. This approach provides a minimum CO_2 content for the reconstructed melt (Figure 5a-d; histograms). Error analysis (Supplementary Material, Appendix 1) indicates that the relative error in minimum CO_2 content determined based on the proportion of vapor in the MI and the CO_2 density in the bubble ranges from about 1 to 20%, and the relative error increases with bubble density and volume percent vapor.

Alternatively, sometimes data are available for MI from the same eruption, and these can be used to approximate the CO_2 content of the glass, as in the case of Kilauea MI studied here. For example, analysis of the glass phase in MI from the Kilauea Iki eruption indicated CO_2 contents ranging from ~0-250 ppm, with one value of 425 ppm, and analyses of the glass phase in MI from Kapoho showed 100-300 ppm (Tuohy et al., in preparation). These analyzed MI are from the same samples used in this study. Similarly, Kilauea Iki MI analyzed by Anderson and Brown (1993) contain 0-300 ppm CO_2, with a single outlier above 700 ppm. These values are similar to the more recent data of Touhy et al. (in preparation). Based on these values, we reconstructed the CO_2 content of the original melt assuming that the glass contains 300 ppm CO_2, representing the maximum reported CO_2 contents of the glass in MI from these eruptions from other studies.

We note that the reconstructed CO_2 content based on some finite amount of CO_2 in the glass is always equal to the CO_2 content estimated by assuming that the glass contains no CO_2, plus the finite amount of CO_2 that is assumed for the glass because of the simplifying assumption that the mass of the bubble is negligible compared to the mass of the glass phase. This means that the reconstructed CO_2 concentration can be determined for any known or assumed concentration of CO_2 in the glass simply by adding the concentration of CO_2 in the glass (in ppm or wt%) to the reconstructed CO_2 concentration that was calculated by assuming that the glass contains no CO_2. This assumption is valid for all of the bubble volumes and CO_2 densities encountered in this study. For example, MI Kap 8 Nat R 2_13 (Table 2) contains 5 volume percent vapor with a CO_2 density of 0.13 g/cm^3. The reconstructed CO_2 concentration of the melt based on the assumption that the glass contains 0 ppm CO_2 is 2,482 ppm. If however, the glass contains 300 ppm, then the reconstructed melt in this MI would contain 2,781 ppm. Thus, the reconstructed CO_2 concentration in the MI in which the glass contains 300 ppm CO_2 is 299 ppm greater than the reconstructed concentration assuming 0 ppm in the glass.

The reconstructed CO_2 concentration for Kilauea Iki MI, assuming that the glass contains 0 ppm CO_2, ranges from 8 to 4,289 ppm (Table 2, Figure 5a; histogram), whereas the CO_2 concentration for Kilauea Iki MI that was estimated by assuming that the glass contains 300 ppm ranges from 308 to 4,589 ppm. Figure 6a shows the proportion of CO_2 in the bubble for the Kilauea Iki MI, estimated by assuming that the glass contains 300 ppm CO_2. For example, the line labeled 50% corresponds to MI for which 50% of all of the CO_2 in the MI (by mass) is contained in the bubble. The calculated proportion of the total amount of CO_2 in the MI that is contained in the bubble ranges from 2 to 93% for the Kilauea Iki eruption.

Similarly, the reconstructed CO_2 concentration for Kapoho ranges from 222 to 2650 ppm (Table 2, Figure 5b), assuming that the glass contains 0 ppm CO_2. The calculated proportion of the total amount of CO_2 in the MI that is contained in the bubble ranges from 42 to 90% for the Kapoho eruption (Fig. 6b), assuming that the glass contains 300 ppm CO_2.

The reconstructed CO_2 concentration for Fuego ranges from 293 to 4,076 ppm (Table 3, Figure 5c), assuming that the glass contains 0 ppm CO_2, whereas the CO_2 content for Fuego MI ranges from 993 to 4,776 ppm assuming that the glass contains 700 ppm CO_2, which represents the upper concentration limit reported by Lloyd et al. (2013) (Fig. 5c). The calculated proportion of the total amount of CO_2 in the MI that is contained in the bubble ranges from 30 to 85% for the Fuego eruption (Fig. 6b), assuming that the glass contains 700 ppm CO_2.

The reconstructed CO_2 concentration for Seguam ranges from 14 to 707 ppm (Table 4, Figure 5d), assuming that the glass contains 0 ppm CO_2, whereas the CO_2 content for Seguam MI ranges from 514 to 1,207 ppm assuming that the glass contains 500 ppm CO_2. The calculated proportion of the total amount of CO_2 in the MI that is contained in the bubble ranges from 3 to 59% for the Seguam eruption (Fig. 6c), assuming that the glass contains 500 ppm CO_2.

Figure 6d shows the relationship between the CO_2 concentration in the glass and the percentage of CO_2 contained in the bubble over the complete range in CO_2 concentrations in the glass that have been observed in MI from the four eruptions considered in this study (Anderson & Brown, 1993; Zimmer et al., 2010; Lloyd et al., 2013; this study). The contours show this relationship for MI containing 0.1, 1 and 10 volume percent vapor and CO_2 densities of 0.01 and 0.1g/cm^3, representing the range of observed values in this study (with the exception of a few MI that contained bubbles with densities ranging up to 0.26 g/cm^3).

Because the CO_2 content of the trapped melt that is calculated assuming that the glass contains no CO_2 represents a minimum value, and because the actual CO_2 content of the trapped melt can be estimated simply by adding the CO_2 content of the glass to the value obtained by assuming that the glass does not contain any CO_2, we can estimate the CO_2 content of the trapped melt for any CO_2 content in the glass using the measured volume percent vapor in the MI and the density of CO_2 in the bubble (Fig. 6d). For example, if the vapor bubble in a MI has a CO_2 density of 0.1 g/cm^3 and occupies 1 volume percent of the MI (or has a CO_2 density of 0.01 g/cm^3 and occupies 10 volume percent of the MI), and if the glass in the MI contains 400 ppm CO_2, then ~50% of the total CO_2 in the MI would be contained in the vapor bubble (see Fig. 6d)

The CO_2 content of the glass in the MI is known. In many cases it is possible to analyze the vapor bubble in the MI by Raman to determine the CO_2 density, and then to determine the volatile content of the glass by FTIR or SIMS, as was done here for several MI from each eruption studied here. For the inclusions that we analyzed by both SIMS/FTIR (glass) and Raman (bubble), we reconstructed the CO_2 content of the trapped melt using a mass balance approach (Esposito et al., 2011) and a correction for PEC. The method is similar to that used above for MI in which the CO_2 content of the glass is unknown, except that in the present case we use a known rather than an assumed (or zero) CO_2 content. The reconstructed CO_2 contents of MI from Kilauea Iki, Kapoho, Fuego, and Seguam Island are listed in Table 5 and shown as data points with error bars in the CO_2 versus H_2O plots on the right side of Figure 5 (a, b, c, and d, respectively).

Based on FTIR analyses by Tuohy et al. (in preparation), the MI from Kilauea Iki contain 50-471 ppm CO_2 in the glass. The reconstructed melts contain up to 624^{+116}_{-183} ppm CO_2 and 48% to 63% of the total CO_2 contained in these MI is in the bubble (Table 5). Figure 5a shows a summary of the volatile contents of the MI from Kilauea Iki: on the left is a histogram depicting minimum CO_2 concentrations calculated based on Raman analysis of the bubbles and assuming that the glass contains no CO_2 (see above); on the right is a plot of the reconstructed values based on our measurements of the CO_2 in the glass and similar measurements made by Anderson and Brown, (1993); also shown are data from MI from Loihi dredge samples (Hauri, 2002), which represent some of the highest concentrations of CO_2 measured *in situ* from MI glasses from Hawaii. Of the 75 Kilauea Iki MI that we analyzed, about 60% contain bubbles with quantifiable CO_2, but only two of these vapor bubble-bearing MI could be analyzed by FTIR. The requirement that MI be polished on two sides for FTIR analysis restricts analysis to only the largest MI, and the larger Kilauea Iki MI were typically crosscut by fractures in the host olivine. Figure 5a shows that approximately half of the Kilauea Iki MI have minimum CO_2 concentrations (based on analysis of the vapor bubble and assuming that the glass contains 0 ppm CO_2) that are higher than CO_2 concentrations in the glass. The range in minimum CO_2 concentrations determined for Kilauea Iki in this study based on analysis of only the vapor bubbles extends to higher values than the CO_2 concentrations of two reconstructed MI that include both CO_2 in the vapor bubble and CO_2 in the glass.

Based on FTIR analyses by Tuohy et al. (in preparation), the Kapoho MI contain 37-294 ppm CO_2 in the glass. After reconstruction, the melts contain up to 1944^{+362}_{-825} ppm CO_2, and 61 to 97% of the total CO_2 contained in the MI is in the bubble (Table 5). Figure 5b shows a summary of the volatile contents of the MI from Kapoho: on the left is a histogram depicting minimum CO_2 concentrations calculated based on Raman analysis of the bubbles and assuming that the glass contains no CO_2 (see above); on the right is a plot of the reconstructed values based on our measurements of the CO_2 in the glass. The amount of CO_2 contained in the bubble and in the glass could be determined for four MI from Kapoho (excluding one anomalous inclusion, see below). All four of these MI have reconstructed CO_2 concentrations that are significantly higher than those obtained by analyzing the glass only, and these reconstructed concentrations are also consistent with those obtained by Raman analysis of the bubbles in the smaller MI in these samples.

After reconstructing the CO_2 contents to include CO_2 contained in the bubble, the CO_2 concentrations of MI from Fuego range from 513^{+46}_{-164} to 2598^{+287}_{-1054} ppm, and 63 to 81% of the total CO_2 in the MI is contained in the bubble (Table 5). Figure 5c shows a summary of the volatile contents of the MI from Fuego: on the left is a histogram depicting minimum CO_2 concentrations calculated based on Raman analysis of the bubbles and assuming that the glass contains no CO_2 (see above); on the right are reconstructed values that include CO_2 contents of the glass obtained in this study and similar measurements made by Lloyd et al., (2013). Although we were only able to reconstruct the trapped-melt compositions of four inclusions using data from both the vapor bubbles and the glass, these reconstructed values are in agreement with the minimum values estimated by Raman analysis of the bubble only. Figure 5c also shows the CO_2 content in the glass for MI with bubbles in which we were unable to quantify the CO_2 density (see above). Although we were able to detect CO_2 in these MI by Raman analysis, these bubbles likely contain significantly less CO_2 than those in the reconstructed MI. These MI could represent trapping of a CO_2-poor melt, or MI in which the quenching rate was too fast to allow exsolved CO_2 in the trapped melt to diffuse into the bubble to produce an equilibrium concentration (pressure), or they might contain carbonates that cannot be recognized.

After reconstruction, Seguam MI contain from 77^{+1}_{-9} to 896^{+102}_{-305} ppm CO_2, and 18% to 93% of the total CO_2 in the MI is in the bubble (Table 5). Figure 5d shows a summary of the volatile contents of the MI from Seguam: on the left is a histogram depicting minimum CO_2 concentrations calculated based on Raman analysis of the bubbles and assuming that the glass contains no CO_2 (see above); on the right is a plot of the reconstructed values based on our measurements of CO_2 in the glass and similar measurements made by Zimmer et al., (2010). Similar to Fuego, the range in minimum CO_2 concentrations is consistent with the range in reconstructed compositions. Figure 5d also shows concentrations of CO_2 in glass in three bubble-bearing MI for which we were unable to quantify the density of CO_2 in the bubble by Raman analysis; in two of these MI, CO_2 was not detected. These bubbles likely represent MI that trapped a melt that had previously undergone significant degassing, or in which carbonates that cannot be recognized have formed, consuming the CO_2.

Having analyzed the CO_2 content of the glass in several of our MI, it is possible to compare the proportion of CO_2 contained in the bubble from this study with results from previous studies of similar MI (Anderson & Brown, 1993; Zimmer et al., 2010; Lloyd et al., 2013) (Fig. 7). For most MI in all four eruptions, our estimate was lower than the value calculated from measurements of both the glass and the bubble – typically by about 20%. This likely reflects the fact that we used the maximum value from the range of measured glass compositions reported by previous studies for each eruption. This was done because the CO_2 concentration in the glass shows a log-normal distribution in some cases (Figure 7b, d), and we wanted to avoid overestimating the proportion of the total CO_2 in the MI that was contained in the bubble (i.e. by using a glass composition that is too low). If we had taken a less conservative approach and used an average value instead, the proportion of CO_2 contained in the bubble would be more similar to the values we calculated from measurements of both the glass and the bubble.

"True" open-system degassing. By directly analyzing the CO_2 contents of the glass and of the bubble and reconstructing the original CO_2 content of the trapped melt, it is possible to determine whether the CO_2 trend represents a "false" or "fictive" degassing path produced by postentrapment decompression or represents inclusion trapping along a "true" open-system degassing path. If the MI glass compositions represent a false degassing path, then the reconstructed CO_2 concentrations would all be the same (or they would overlap within analytical error). If the MI record "true" degassing behavior, then the reconstructed CO_2 contents should vary systematically as predicted by the decrease in CO_2 solubility with decreasing pressure. . Although the error associated with the mass balance calculations is substantial (Fig. 5), the reconstructed CO_2 contents vary significantly for each eruption. Therefore, we conclude that these MI could be recording open-system degassing trends for each eruption, but depths and pressures calculated based only on the MI glass composition would be incorrect. We emphasize that it would be possible to determine if the MI were trapped along an open-system degassing path with greater certainty if data were available for individual Melt Inclusion Assemblages

(MIA) (Bodnar and Student, 2006) that could be placed into a rigorous paragenetic sequence, and if CO_2 contents within individual MIA were consistent, but decreased systematically from early to late MIA (Esposito et al., 2014).

Revised depths and pressures of formation

The trapping pressures and depths for the inclusions from Kilauea, Fuego and Seguam have been revised based on our new volatile data, using VolatileCalc (Newman and Lowenstern, 2002). Table 5 shows a comparison of the trapping pressures and depths (assuming 3.5 km/kbar) before and after reconstructing the CO_2 contents for the Kilauea, Fuego, and Seguam samples, and Figure 5 (right side of Figs. 5a-d) shows the CO_2 contents before and after mass balance reconstruction. The revised trapping pressures for Fuego and Seguam MI are discussed below; the MI from Kilauea are discussed by Tuohy et al. (in preparation).

Using the reconstructed CO_2 concentrations for Fuego MI, the calculated trapping pressures span a range from 2.6 to 6.0 kbars, which corresponds to depths of 9 to 22 km. For comparison, based on the volatile content of only the glass yields a range in trapping pressures of 1.9 to 2.5 kbar, which corresponds to depths of 7 to10 km. Lloyd et al. (2013) report trapping depths of 7 – 8 km, and Rose et al. (1978) suggest that crystallization could have begun between 5 and 10 km; both estimates are based on melt-volatile solubility. Using an alternate method, Roggensack (2001) predicted a range from <3-13 km for trapping depths based on a crystal size indicator.

The calculated trapping pressures for the Seguam MI based on the reconstructed CO_2 concentrations extend up to 3.4 kbar, corresponding to a depth of ~12 km. For comparison, the trapping pressures calculated using volatile concentrations measured from the glass only are 0.9 to 2.5 kbars, corresponding to depths of 3 – 9 km. The revised pressures and depths are consistent with Jicha et al. (2006) who predicted pressures of 3-5 kbar based on estimated depths (~10-15 km) at which basalt parent magmas began to crystallize, as inferred from isotopic data and modal mineralogy.

Carbonate Phases in Melt Inclusions

As noted above, carbonates were commonly observed in the bubbles in MI from Seguam and Fuego, and to a lesser extent in MI from Kapoho. The occurrence of carbonates (and other minerals) on the bubble wall has been reported for MI from various volcanic settings (Kamenetsky and Kamenetsky, 2010 and references therein). However, such phases are usually not reported in studies that focus on volcanic degassing behavior (e.g., Kamenetsky et al., 2007). The presence of carbonate minerals on the bubble wall implies that analysis of the glass phase and vapor bubbles in MI may not completely account for all of the C that was originally trapped in a MI as dissolved CO_2.

The presence of carbonates in the MI from Fuego and Seguam also raises questions concerning the relative rarity of detectable CO_2 in the vapor phase of these MI. While CO_2 was detected in a smaller proportion of the bubbles in MI from Fuego and Seguam as compared to the samples from Kapoho, carbonate minerals were detected in a greater proportion of MI from Fuego and Seguam, compared to those from the two Kilauea eruptions. In all four MI where carbonate was detected in vapor bubbles from Kapoho, CO_2 was also detected (Table 2). However, CO_2 was detected in the vapor bubbles in only two of the sixteen MI from Fuego volcano in which carbonate was also detected (Table 3). Similarly, CO_2 was detected in the vapor bubble in only two of the nine MI from Seguam in which carbonates were detected by Raman analysis or by visual inspection (Table 4, Figure 3e,f). Because of these discrepancies, it is likely that a significant portion of the CO_2 that exsolved from the melt after the Fuego and Seguam MI were trapped is sequestered in carbonate phases.

Although it is beyond the scope of the present study to precisely quantify the contribution of carbonates to the CO_2 budget of the studied MI, we can examine the effect of secondary carbonate produced from CO_2 that exsolved from the melt on the reconstructed CO_2 content of the MI. We can then determine whether the amount of carbonate observed is likely to have a significant effect on our estimated CO_2 contents. To accomplish this, we assume that C contained in the carbonates was originally present as CO_2 in the vapor bubble, and that carbonate formed as a result of reaction of CO_2 in the fluid with the surrounding glass (or melt). Moreover, as we can estimate the volume of the vapor bubble with reasonable precision, it is convenient to relate the volume of carbonate in the MI to the vapor bubble volume. For example, the volume of a carbonate crystal that would contain the same mass of C as a vapor bubble with a given CO_2 density can be calculated as a function of the molar mass of CO_2 ($\overline{m}_{CO_2}$), the molar mass of the carbonate mineral ($\overline{m}_{carb}$), and the density of the carbonate crystal (ρ_{carb}):

$$V_{carb}^{\%} = \frac{\overline{m}_{carb}}{\overline{m}_{CO_2}\rho_{carb}}\rho_{CO_2}$$

where ρ_{CO_2} and $V_{carb}^{\%}$ are the density of CO_2 in the bubble and the size (volume)of the carbonate phase relative to the volume of the bubble. For example, a CO_2 vapor bubble with a density of 0.25 g/cm^3 would contain the same amount of C as a calcite crystal with a volume that is ~30% of the bubble volume. It is likely that the bubbles in our MI contain less than 30 volume percent of carbonate. A more likely maximum volume proportion (calcite volume divided by bubble volume) is 0.1% to 1%. This volume proportion of calcite corresponds to a CO_2 vapor bubble with a density between 0.001 and 0.01 g/cm^3, and this range is consistent with the lower end of the range in CO_2 densities we have measured.

Based on observations of carbonate-bearing bubbles (Figure 3 e-f, Kamenetsky et al, 2007) the carbonate phase would likely be distributed across the glass-bubble interface in the form of numerous small crystals rather than as a single, larger crystal. For this reason, estimating the volume proportion of carbonate in a MI is challenging unless both the number of carbonate crystals and the volume of each crystal can be determined. Based on inspection of Figure 3f, it appears that the largest of the carbonate crystals has a diameter that is approximately 1/20th of the diameter of the bubble (~1.8 μm). If all of the carbonate crystals were of similar size, then an area fraction of the bubble can be approximated by comparing the area of n circles with diameters equal in diameter to each individual carbonate crystal so that n is the number of spheres it would take to create the total volume of the carbonate. For example, if a bubble contains 2% carbonate crystals (by volume), each with a diameter 1/20th of the bubble diameter, then 10% of the bubble surface would be covered by carbonate crystals.

By visual inspection, it appears that about 10% of the surface of the bubble in Figure 3 is covered by carbonate crystals that range in diameter from 1/60th to 1/20th of the diameter of the bubble. This corresponds to 0.66 to 2.0 volume percent of carbonate in the bubble and an equivalent CO_2 density ranging from 0.008 to 0.024 g/cm^3. For a vapor bubble that occupies 3 volume percent of the inclusion, this corresponds to a range in minimum CO_2 content of 89 to 267 ppm. If the carbonate-bearing bubble is contained within an inclusion that contains 300 ppm CO_2 in the glass, similar to the concentrations determined by SIMS and FTIR for the MI in this study, then 23 to 47% of the "CO_2" in the MI would be contained in the carbonates (ignoring any CO_2 that may be in the bubble as a vapor).

This "visual inspection" method of quantifying carbonates is intended to demonstrate that the amount of "CO_2" in the carbonates is comparable to the amount of CO_2 contained in a relatively low density (~0.01 g/cm^3) bubble. A more precise method for measuring carbonate crystal volumes is required to further quantify the amount of C contained in the carbonate crystals. For example, scanning electron microscopy (e.g. Kamenetsky et al., 2002) could provide a better approximation of the size of individual carbonate crystals and the fraction of the bubble surface area that they cover, if the bubble is exposed by polishing or ion milling (and if carbonate crystals are not destroyed or lost during polishing). Alternatively, X-ray microtomography (e.g. Smith et al., 2013) could be used to directly measure the volume of carbonate without exposing the bubble; however it is not clear whether the resolution of this technique would allow precise measurements of carbonate crystals that are 10s of nm in diameter or smaller.

Thermal expansion in MI

Most of the MI that we have studied show a relatively uniform 3 volume percent vapor, even though densities of CO_2 in the bubbles vary over a wide range. This is to be expected as the bubble volumes are controlled by the difference in thermal expansion between the trapped melt and the host phenocryst during cooling from the trapping temperature to T_{glass}, rather than by the amount of CO_2 contained in the bubble. If this is the case, then the volume percent vapor to be expected in any melt inclusion in which the volume change of the host and the glass are known as a function of temperature may be estimated. To demonstrate this principle, we calculated the volume change of the melt and host mineral as a function of temperature for MI hosted by a variety of minerals. We note that, although it is relatively straightforward to calculate the differential shrinkage of a MI and its host crystal, the rate of cooling can have a profound effect on shrinkage bubble volume, and an "ideal" shrinkage bubble volume may not be representative in some cases (e.g. Lowenstern 1994b).

To calculate the volume change of the host mineral, we used thermal expansivity data for forsterite (Bouhifd et al., 1996), anorthite (Hovis et al., 2010; Anorthite 137041), clinopyroxene (Hugh-Jones, 1997; $MgSiO_3$), orthopyroxene (Hugh-Jones, 1997; $MgSiO_3$), alkali feldspar (Hovis et al., 2010; Ca-K Feldspar 8817), and quartz (Kozu & Takane, 1929). To calculate the volume change of the melt, we used reported compositions of MI contained in olivine (Zimmer et al. 2010; sample SEG 0706), plagioclase (Severs et al., 2009; Plag 3), clinopyroxene (Severs et al., 2009; Cpx 8), orthopyroxene (Severs et al., 2009; Opx 3), alkali feldspar (Yang and Bodnar; sample B82-6a), and quartz (Anderson et al., 2000; 5D-Lu). The molar volume of the melt contained in each inclusion was calculated using thermodynamic data compiled by Spera (2000) from Lange & Carmichael (1990), Lange (1997), and Ochs and Lange (1997). The relative volume change of the glass was calculated as V/V_0 – the reciprocal of the melt density normalized to the density at the trapping temperature. We compared the calculated melt volume change to the empirically-derived thermal expansion of the host minerals and calculated the size (volume proportion) of the bubble as the difference in thermal contraction between the melt and the host phase. An Excel-based spreadsheet to implement the calculation procedure described above is available in supplementary material and on the following websites: [http://www.ldeo.columbia.edu/~egazel/] and [http://www.geochem.geos.vt.edu/fluids/].

Figure 8 shows the results of the calculation described above and the mineral expansion and melt composition data used for each example. The volumes of the melt and the host crystal are normalized to their initial values at the trapping temperature (V/V_0). Isochores of volume proportion bubble show the increase in bubble size with decreasing temperature as the difference in thermal expansion of the host and the melt. Once the MI has cooled below T_{glass} the volume of the bubble is "locked in" and the size should remain constant with further cooling to ambient conditions (e.g., Webb, 1997).

The range in bubble volumes (volume percent) that we observed can be explained by a range in T_{glass} and varying trapping temperatures; this range is also consistent with the bubble volumes that we observed in our MI (Figure 8a). We calculated the bubble volume for a MI trapped in olivine using a melt composition reported by Zimmer et al. (2010). We assumed that the MI was trapped at 1200°C and that T_{glass} was between 900°C and 700°C. For T_{glass} = 700°C, olivine contracts by 2% and the melt contracts by 7%; this produces a vapor bubble occupying 5 volume percent after 500°C of cooling. For T_{glass} = 900°C, olivine contracts by 1% and the melt contracts by 4%; this produces a vapor bubble occupying 3 volume percent of the MI. Thus, we estimate that basaltic MI trapped in olivine at 1200°C should contain 3 to 5 volume percent vapor, in agreement with the values calculated by Riker (2005) for Mauna Loa melt inclusions (see also Wallace et al., in review). This suggests that MI in olivine containing bubbles that occupy >5 volume % of the MI likely trapped melt + vapor. However, more silicic glass compositions might be expected to contain relatively smaller bubbles. Thus, we recommend that bubbles be screened for heterogeneous trapping both by comparing bubble volume with MI volume and by considering bubble volume as a function of melt and mineral thermal contraction data.

We similarly calculated expected vapor bubble sizes for MI trapped in anorthite, orthopyroxene, clinopyroxene, alkali feldspar, and quartz (Figure 8b-f). In general (with quartz as an exception; see below) all of the minerals contract by about 1% (feldspars) to 2% (olivine and pyroxenes) over a 500°C temperature range. The smallest bubbles are predicted to occur in

MI trapped in alkali feldspar because rhyolitic melt contracts less during cooling compared to more mafic compositions; the largest vapor bubbles are expected to occur in orthopyroxene because basaltic melt contracts by the largest amount during cooling.

For the MI hosted by anorthite (Figure 8b), we estimated the amount of melt contraction using two different melt compositions (Severs et al. 2009): one from a MI hosted by plagioclase, and the other hosted by clinopyroxene. This was done to illustrate the range of bubble volumes that could be produced because plagioclase feldspars could potentially trap MI from a wide range of melt compositions. The more mafic OPX (8) melt contracts about three times more than the Plag (3) melt over the same temperature interval (i.e. for the same temperature, the bubble volume is three times as large). However, a MI trapping a more evolved melt would likely have a lower trapping temperature and a lower T_{glass}, and the cooling interval would be smaller.

Because water has a pronounced effect on the rheology of melts, we calculated melt volumes for both a basaltic MI and a rhyolitic MI with and without water (Figure 8a, e). In both cases, the anhydrous melt shrinks less than the hydrous melt. The effect of water is much less pronounced for the basaltic melt, and the melt volume curves almost coincide (Figure 8a); the effect of water is significantly more pronounced for the rhyolitic melt (Figure 8e). This difference is the result of the relative abundance of SiO_2 and H_2O in the rhyolite composition we used in our model. SiO_2 expands negligibly with increasing temperature in silicate melts and H_2O expands more than any major element oxide component (except for K_2O) Spera (2000). We also note that a dry melt should have a higher T_{glass}, and would experience a smaller cooling interval (ΔT) before the bubble volume is “locked in”. For both of these reasons, MI that trap a dry melt should generally contain smaller bubbles, compared to MI that trap a hydrous melt.

Predicting the bubble size in MI trapped in quartz is considerably more challenging because the MI may pass through the α/β quartz transition after trapping and before the glass transition temperature is reached. The effect of the α/β quartz transition on bubble nucleation and growth can sometimes be observed during heating experiments (e.g. Clocchiatti, 1975; Lowenstern, 1994b). At 1 atm, the α/β quartz transition occurs at 573°C, and this temperature is likely higher than T_{glass} for a hydrous rhyolitic melt (Figure 8f). Figure 8f shows the variation in relative vapor bubble volume over a range of temperatures spanning the α/β transition for a MI trapped in quartz at 1000°C. Using a melt composition from Anderson et al. (2000) and quartz thermal expansion data from Kozu & Takane (1929), we estimate that the MI would contain ~2.8 volume % vapor at 574°C. When the cooling path passes through the α-β transition, the quartz volume will abruptly decrease by ~0.8%. With further cooling from 573°C to ~400°C, the quartz volume decreases more than the melt volume (i.e. the bubble shrinks over this interval). Thus, the largest possible bubble (~2.8 volume percent) occurs when T_{glass} is reached just before the α-β quartz transition.

Predicting volumes of vapor bubbles for MI trapped in quartz is further complicated by the effect of water. The melt that we used in our calculation contains ~5 wt% H_2O. If an anhydrous melt is assumed, the melt volume curve (V/V_0) intersects the quartz volume curve (figure 8f) at the α-β quartz transition. This indicates that MI containing dry melts in quartz should not contain a vapor bubble. It is also possible that a MI containing an anhydrous melt might have a T_{glass} that is above the α-β quartz transition temperature so that it could form a small (<1 volume percent) bubble and then become a glass before crossing the α-β quartz transition. However, such a small bubble may not be able to overcome the force of surface tension that controls the lower limits for bubble nucleation (Lowenstern, 1994b).

Reconstruction of MI volatile budgets using PVTX data for melt-volatile systems

By calculating the differential contraction between a MI and the mineral host (as we have done above) it can be shown that the volume proportion of a MI occupied by a vapor bubble is controlled by the difference in thermal expansivity between the glass and the host mineral. However, the density of CO_2 that is contained in the bubble is also controlled by the amount of CO_2 that is able to diffuse into the bubble before crossing the glass transition temperature. Under ideal conditions, the amount of CO_2 contained in the vapor bubble would equal the amount required to maintain the equilibrium vapor pressure for the volatile saturated melt in the MI. However, if the mass of CO_2 transferred into the bubble is limited by diffusion, the amounts of CO_2 that we have measured by Raman spectroscopy may not represent the equilibrium amounts. Using data for Ar diffusion as a function of P, T, and H_2O content, which is almost identical to CO_2 diffusion (see references in Zhang et al., 2007, and references therein), we can calculate a "characteristic time" (e.g. Watson et al., 1982) required for CO_2 to diffuse across a MI to a vapor bubble. The diffusivity of CO_2 is strongly dependent on temperature and H_2O content; the sensitivity to pressure is comparatively minor. For example, CO_2 has a diffusivity of ~7.5×10^{-12} m^2/s in a melt that contains 0.5 wt% H_2O at 1200°C (e.g. Kilauea), but at T_{glass} (~800°C) the diffusivity is ~1×10^{-13} m^2/s. Assuming a diffusion length of 50 μm, which represent the average diameter of MI studied here (Tables 2-4), and a diffusivity of ~7.5×10^{-12} m^2/s, it would take ~5 minutes for CO_2 to diffuse from one side of the MI to the other side. However, at T_{glass} it would take ~7 hours for CO_2 to diffuse the same distance. If the H_2O content of the melt is increased to 4 wt% (e.g. Feugo, Seguam), the diffusivity increases by an order of magnitude such that at T_{glass} CO_2 could diffuse the same distance in ~20 minutes. This example indicates that it is not possible for relatively dry MI like those from Kilauea to exsolve a significant amount of CO_2 into the bubble if they are cooled from the trapping temperature to T_{glass} over a period of less than a few minutes. The amounts of CO_2 that we observe in the bubble indicate that the MI from Kilauea must have cooled by a few hundred degrees over a period of minutes to hours. We note that melt inclusions at Kilauea (and presumably elsewhere) have experienced two stages of cooling (Anderson and Brown, 1993). The first is between the trapping temperature and immediately pre-eruption, while the second stage of cooling is during eruption. At Kilauea the first stage of cooling is commonly on the order of 50-100°C, but the duration of this cooling event is basically unknown. However, trace elements in Kilauea Iki MI broadly suggest that this first stage of cooling could have occurred in as little as a week, and up to a few hundred years. The second stage of cooling at Kilauea happens in the eruptive plume of fire fountains, and cooling may happen over seconds. As a result, almost no additional CO_2 is transferred from melt to vapor during eruptive cooling, and therefore the CO_2 that is in the bubble was exsolved from the melt during the pre-eruptive stage. However, because CO_2 diffusion rates are faster in H_2O-bearing melts than in dry melts, CO_2 loss to the vapor bubble in MI containing H_2O-rich melts (i.e., Fuego and Seguam) is less sensitive to cooling rates, compared to H_2O-poor melts.

In this study, we determined the amount of CO_2 contained in the bubbles of bubble-bearing MI based on *in situ* Raman analysis. However, the composition and density of vapor bubbles in MI may alternatively be estimated using information on the solubility of volatiles in the melt combined with an equation of state (EOS) for the fluid. With this method, the volatile content of the glass obtained by SIMS or FTIR analysis is used to estimate the total pressure $[P_{CO2} + P_{H2O}]$ in the MI at the moment that the volatile content of the melt was “locked in” during cooling – this is generally assumed to occur at T_{glass}. Then, using a volatile solubility model such as VolatilCalc (Newman & Lowenstern, 2002) or the model of Papale et al. (2006), the composition of the vapor phase that is in equilibrium with the melt at the calculated pressure and T_{glass} is determined. Finally, the density of the vapor phase is estimated using either the Ideal Gas Law (IGL) or some other Equation of State (EOS).

As an example of the application of this method, Shaw et al. (2008) calculated the volatile content of MI from the Mariana Arc and estimated that ~80% of the CO_2 (and about 2% of the H_2O) in the MI was contained in the bubble. These workers used the IGL ($n = PV/RT$) to estimate the fluid density. Here, we have reconstructed the CO_2 contents for our MI using the IGL as well as a commonly-used EOS (Mao et al., 2009). Pressures in the MI were estimated using VolatileCalc (Newman & Lowenstern, 2002), and vapor bubble volumes were calculated from the measured bubble diameters. We assumed $T_{glass} = 700\ ^{o}C$ for Fuego and Seguam MI and 825 ^{o}C for Kilauea Iki and Kapoho MI (Bouhifd et al., 2006). The amount (mass) of CO_2 in the bubble was calculated using the IGL and the mole fraction of CO_2 in the vapor predicted by the Newman and Lowenstern (2002) solubility model. The reconstructed CO_2 concentrations were calculated using the same mass balance approach described above, and the results are shown in Figure 9a.

For comparison, we also reconstructed the MI compositions using the EOS of Mao et al. (2009, hereafter the “Mao EOS”) that was developed to predict PVT properties of mixed H_2O-CO_2 fluids. The reconstruction used the same T_{glass}, pressures, and vapor compositions as described above. The calculated density was then used to determine the amount of CO_2 and H_2O in the bubble, again using the vapor composition predicted by VolatileCalc. Figure 9b shows reconstructed CO_2 concentrations estimated using the Mao EOS compared to those calculated using the IGL. At the PTX conditions used, both methods predict similar results.

Our comparison suggests that reconstructing the CO_2 content of a MI using the IGL or some other EOS overestimates the CO_2 concentrations in the melt by up to a factor of 6, compared to values estimated based on Raman analysis (Figure 9a). We suggest that this difference reflects the fact that the Raman technique is measuring the actual amount of CO_2 that is contained in the vapor bubble, whereas the IGL method assumes that the bubble size and the amount of CO_2 it contains represent equilibrium between the melt and the vapor. As noted by Anderson and Brown (1993) and Riker (2005), a limitation of using the IGL to estimate the density of the vapor phase is that the MI undergoes quenching on a timescale that is too fast for volatiles to diffuse from the melt and into the bubble to maintain equilibrium between the volatile content of the melt and the volatiles in the bubble.

A recent detailed mapping of the volatile distribution in MI and the surrounding host phase has provided evidence to support the heterogeneous distribution of volatiles in some MI (Esposito et al., 2014). Recent experiments by Pichavant et al. (2013) suggest that this could result from the slow CO_2 diffusion to produce heterogeneities on μm length scales, which controls the degassing mechanism in operation. Both of these studies support the interpretation that if the size of the bubble does not represent its equilibrium pre-eruptive size, then the amount of CO_2 contained in the bubble is less than would be predicted assuming equilibrium between the melt and the vapor. In summary, if one has data for the volatile content of the glass from FTIR or SIMS analysis and then uses the IGL or some other EOS to reconstruct the bulk volatile content of the melt, it is likely that the predicted volatile content would be higher than the true concentration, perhaps by about one-half of an order of magnitude, unless one correctly accounts for the rapid expansion that occurs during eruption and cooling (Wallace et al., in review).

IMPLICATIONS

In this study, we measured both the amount of CO_2 contained in the vapor bubble and in the glass for a suite of bubble-bearing melt inclusions (MI). We observed that, in many cases, most of the CO_2 in a bubble-bearing MI is contained in the bubble. Based on our analysis of over 230 bubble-bearing MI, we agree with the conclusions of other studies (Anderson and Brown, 1993; Shaw et al., 2008; Esposito et al., 2011; Bucholz et al., 2013; Hartley et al., 2014; Wallace et al., in review), that CO_2-bearing vapor bubbles are common in MI from volcanic systems. Moreover, estimates of the total volatile budget of the MI that do not include the CO_2 contained in the bubble will significantly underestimate the total amount of CO_2 in the MI. In addition, failure to account for CO_2 in vapor bubbles has the potential for producing false degassing trends that are similar to those resulting from open system degassing. Using the mass balance approach described by Esposito et al. (2011) that we have applied in this study, the complete volatile budget of the MI can be determined if the amount of CO_2 contained in the bubble is determined and added back into the melt.

ACKNOWLEDGEMENTS

This project was partially supported by the Department of Geosciences at Virginia Tech and by a Geological Society of America student awards to LM. Sampling and analysis of Kilauea MI by RT was supported by a Jack Kleinman Grant from the U.S. Geological Survey and an ExxonMobile Research Science Grant. We thank Jianhua Wang for expert maintenance of the Carnegie ion probe. Thorough reviews and suggestions by Elizabeth Johnson, Jake Lowenstern and Nicole Métrich significantly improved the quality of the manuscript. Discussions with Matt Steele-MacInnis contributed greatly to the development of the calculator for reconstructing MI volatile contents. This material is based upon work supported in part by the National Science Foundation under Grants no. EAR-1019770 to RJB, EAR- 1201903 to EG, and EAR- 0948533 to TP, and by the Deep Carbon Observatory.

REFERENCES

Anderson, A.T. and Brown, G.G. (1993) CO_2 contents and formation pressures of some Kilauean melt inclusions. American Mineralogist, 78, 794-803.

Andersen, T., O'Reilly, S.Y., and Griffin, W.L. (1984) The trapped fluid phase in upper mantle xenoliths from Victoria, Australia: implications for mantle metasomatism. Contributions to Mineralogy and Petrology, 88, 72-85.

Anderson, A.T., Davis, A.M., and Lu, F. (2000) Evolution of Bishop Tuff rhyolitic magma based on melt and magnetite inclusions and zoned phenocrysts. Journal of Petrology, 41 (3), 4449-473.

Audétat, A., and Lowenstern, J.B. (2014) 13.6 - Melt Inclusions. In H.D. Holland, and K.K. Turekian, Eds. Treatise on Geochemistry (Second Edition), p. 143-173. Elsevier, Oxford

Bodnar, R.J. and Student, J.J. (2006) Melt inclusions in plutonic rocks: Petrography and microthermometry. Melt Inclusions in Plutonic Rocks (J. D. Webster, ed.), Mineralogical Association of Canada, Short Course 36, 1-26.

Bouhifd, M.A., Fiquet, A.G., and Richet, P. (1996) Thermal expansion of forsterite up to the melting point. Geophysical Research Letters, 23, 10, 1143-1146.Bouhifd, M. A., Besson, P., Courtial, P., Ge´rardin, C., Navrotsky, A., and Richet, P. (2007) Thermochemistry and melting properties of basalt. Contributions to Mineralogy and Petrology, 153, 689–698.

Borisov, A.A. and Shapkin, A.I. (1990). A new empirical equation rating Fe3+/Fe2+ in magmas to their composition, oxygen fugacity, and temperature. Geochemistry International, 27, 111-116.

Bucholz, C.E., Gaetani, G.A., Behn, M.D., and Shimizu, N., (2013) Post-entrapment modification of volatiles and oxygen fugacity in olivine-hosted melt inclusions. Earth & Planetary Science Letters, 374, 145-155.

Burke, E.A.J. (1994) Raman microspectrometry of fluid inclusions. In: De Vivo, B., Frezzotti, M.L. (Eds.), Fluid Inclusions in Minerals: Method and Applications. Short Course of Working Group (IMA) "Inclusions in Minerals", Virginia Polytechnic Institute and State University, pp. 25–44.

Burnham, W.C. and Ohmoto, H. 1980. Late-stage processes of felsic magmatism. Society of Mining Geologists of Japan, Special Volume 8, 1-11.

Burruss, R.C. (2003) Raman spectroscopy of fluid inclusions. In: Samson, I., Anderson, A., Marshall, D. (Eds.), Fluid inclusions: analysis and interpretation, Mineralogical Association of Canada, short course series, 32, pp. 279–289.

Canil, D. (2002) Vanadium in peridotites, mantle redox and tectonic environments: Archean to present. Earth & Planetary Science Letters, 195, 75-90.

Cervantes, P., Kamenetsky, V., and Wallace, P. (2002). Melt inclusion volatile contents, pressures of crystallization for Hawaiian picrites, and the problem of shrinkage bubbles. EOS, Transactions, American Geophysical Union 83, F1495-F1496.

Cervantes, P. and Wallace, P. (2003) Magma degassing and basaltic eruption styles: a case study of ~2000 year BP Xitle volcano in central Mexico. Journal of Volcanology and Geothermal Research, 120, 249-270.

Clocchiatti, R. (1975) Les inclusions vitreuses des cristaux de quartz: étude optique, thermo-optique et chemique Applications géologiques. Mémoires de la Société Géologique de France, 122, 96 p.

Danyushevsky L.V., McNeill, A.W., and Sobolev, A.V. (2002) Experimental and petrological studies of melt inclusions in phenocrysts from mantle-derived magmas: an overview of techniques, advantages and complications. Chemical Geology, 183, 5-24.

Danyushevsky, L.V. and Plechov, P. (2011) Petrolog3: Integrated software for modeling crystallization processes. Geochemistry, Geophysics, Geosystems, 12, 7, 32 p.

Dixon, J.E., Stolper, E.M., and Holloway, J.R. (1995) An experimental study of water and carbon dioxide solubilities in mid-ocean ridge basaltic liquids. Part I: Calibration and solubility models. Journal of Petrology, 36 (6), 1607-1631.

Esposito, R., Bodnar, R.J., Danyushevsky, L.V., de Vivo, B., Fedele, L., Hunter, J., Lima, A., and Shimizu, N. (2011) Volatile evolution of magma associated with the Solchiaro eruption in the Phlegrean Volcanic District (Italy). Journal of Petrology, 52 (12), 2431-2460.

Esposito, R., Hunter, J., Schiffbauer, J., Shimizu, N. and Bodnar, R.J. (2014) An assessment of the reliability of melt inclusions as recorders of the pre-eruptive volatile content of magmas. American Mineralogist, 99, 976-998.

Fall, A., Tattitch, B., and Bodnar, R.J. (2011) Combined microthermometric and Raman spectroscopic technique to determine the salinity of H_2O–CO_2–NaCl fluid inclusions based on clathrate melting. Geochimica et Cosmochimica Acta, 75, 951-964.

Ford, C.E., Russell, D.G., Craven, J.A., and Fisk, M.R. (1983). Olivine-liquid equilibria; temperature, pressure and composition dependence of the crystal/liquid cation partition coefficients for Mg, Fe2+, Ca and Mn. Journal of Petrology 24, 256-265.

Frezzotti, M.L., Tecce, F., and Casagli, A. (2012) Raman spectroscopy for fluid inclusion analysis. Journal of Geochemical Exploration, 112, 1-20.

Gaetani, G., O'Leary, J., and Shimizu, N. (2012) Post-entrapment changes to H_2O and CO_2 in olivine-hosted melt inclusions. Mineralogical Magazine, 75, 879.

Gazel, E., Plank, T., Forsyth, D.W., Bendersky, C., Lee, C-T.A., and Hauri, E.H. (2012) Lithosphere versus asthenosphere mantle sources at the Big Pine Volcanic Field, California. Geochemistry, Geophysics, Geosystems, 13, 1-25.

Hartley, M.E., Maclennan, J., Edmonds, M., and Thordarson, T. (2014) Reconstructing the deep CO2 degassing behavior of large basaltic fissure eruptions. Earth and Planetary Science Letters, 393, 120-121.

Hauri, E. (2002) SIMS analysis of volatiles in silicate glasses, 2: isotopes and abundances in Hawaiian melt inclusions. Chemical Geology, 183, 115-141.

Hauri, E.H., Wang, J., Dixon, J.E., King, P.L., Mandeville, C., and Newman, S. (2002) SIMS Investigations of volatiles in silicate glasses, 1: Calibration, matrix effects and comparisons with FTIR, Chemical Geology 183, 99-114.

Helo, C., Longpré, M.A., Shimizu, N., Clague, D.A., and Stix, J. (2011) Explosive eruptions at mid-ocean ridges driven by CO_2-rich magmas. Nature Geoscience, 4, 260-263.

Hovis, G.L., Medford, A., Conlon, M., Tether, A., and Romanoski, A. (1997) Principles of thermal expansion in the feldspar system. Journal of Petrology, 183, 87-98.

Hugh-Jones, D. (1997) Thermal expansion of MgSiO3 and FeSiO3 ortho- and clinopyroxenes. American Mineralogist, 82, 689–696.

Jicha, B.R. and Singer, B.S. (2006) Volcanic history and magmatic evolution of Seguam Island, Aleutian Island arc, Alaska. GSA Bulletin, 118, 7/8, 805-822.

Johnson, E.R., Wallace, P.J., Cashman, K.V., Granados, H.D., and Kent, A.J.R. (2008) Magmatic volatile contents and degassing-induced crystallization at Volcán Jorullo, Mexico: Implications for melt evolution and the plumbing systems of monogenetic volcanoes. Earth and Planetary Science Letters, 269, 478-487.

Kamenetsky, V.S. and Kamenetsky, M.B. (2010) Magmatic fluids immiscible with silicate melts: examples from inclusions in phenocrysts and glasses, and implications for magma evolution and metal transport. Geofluids, 10, 293-311.

Kamenetsky, V.S., Davidson, P., Mernagh, T.P., Crawford, A.J., Gemmell, J.B., Portnyagin, M.V., and Shinjo, R. (2002) Fluid bubbles in melt inclusions and pillow-rim glasses: high-temperature precursors to hydrothermal fluids? Chemical Geology, 183, 349-364.

Kamenetsky, V.S., Pompilio, M., Métrich, N., Sobolev, A.V., Kuzmin, D.V., and Thomas, R. (2007) Arrival of extremely volatile-rich high-Mg magmas changes explosivity of Mount Etna. Geology, 35 (3), 255-258.

Kawakami, Y., Yamamoto, J., and Kagi, H. (2003) Micro-Raman densimeter for CO_2 inclusions in mantle-derived minerals. Applied Spectroscopy, 57, 1334-1339.

Klein, F.W., Koyanagi, R.Y., Nakata, J.S., and Tanigawa, W.R. (1987) Volcanism in Hawaii: USGS Professional Paper 1350 (eds, Drecker, R. W., Wright, T. L., Stauffer, P. H.) 2. 1019-1185.

Kozu, S. and Takane, K. (1929) Influence of temperature on the axial ratio, the interfacial angle, and the volume of quartz. Scientific Reports of Tohoku University 3 (3rd series) 239-246.

Lange, R.A. (1997) A revised model for the density and thermal expansivity of K_2O-Na_2O-CaO-MgO-Al_2O_3-SiO_2-liquids from 700 to 1900 K: Extension to crustal magmatic temperatures. Contributions to Mineralogy and Petrology, 130, 1-11.

Lange, R.A. and Carmichael, I.S.E. (1987). Densities of Na_2O-K_2O-MgO-MgO-FeO-Fe_2O_3-Al_3O_3-TiO_2-SiO_2 liquids: New measurements and derived partial molar properties. Geochimica et Cosmochimica Acta 51, 2931-2946.

Lange, R.A., Carmichael, I.S.E. (1990) Thermodynamic properties of silicate liquids with emphasis on density, thermal expansion, and compressibility. Reviews in Mineralogy, 24, 25-59.

Liu, Y., Anderson, A.T., Wilson, C.J.N., Davis, A.M., and Steele, I.M. (2006) Mixing and differentiation in the Oruanui rhyolitic magma, Taupo, New Zealand: Evidence from volatiles and trace elements in melt inclusions. Contributions to Mineralogy and Petrology, 151, 71-87.

Lloyd, A.S., Plank, T., Ruprecht, P., Hauri, E.H., and Rose, W. (2013) Volatile loss from melt inclusions in pyroclasts of differing sizes. Contributions to Mineralogy and Petrology, (published online) online 28 September 2012.

Lowenstern, J.B. (1994a) Dissolved volatile concentrations in an ore-forming magma. Geology, 22, 893-896.

Lowenstern. J.B. (1994b) Chlorine, fluid immiscibility, and degassing in peralkaline magmas from Pantelleria, Italy. American Mineralogist, 79, 353-369.

Lowenstern, J.B. (1995) Applications of silicate-melt inclusions to the study of magmatic volatiles. In: Thompson, J. F. H. (ed.) Magmas, fluids and ore deposition: Mineralogical Association of Canada, Short Course 23, 71-99.

Lowenstern, J.B. (2003) Melt inclusions come of age: Volatiles, volcanoes, and Sorby's legacy. in Melt inclusions in Volcanic Systems, De Vivo B & Bodnar RJ, Eds., Elsevier Amsterdam, 1-21.

Mangiacapra, A., Moretti, R., Rutherford, M., Civetta, L., Orsi, G., and Papale, P. (2008) The deep magmatic system of the Campi Flegrei caldera (Italy). Geophysical Research Letters, 35, 1-6.

Mao, S., Duan, Z., and Hu, W. (2009) A vapor-liquid phase equilibrium model for binary CO2-H2O and CH4-H2O systems above 523 degree C for application to fluid inclusions. The Journal of Supercritical Fluids 50, 13-21.

Massare, D., Métrich, N., and Clocchiatti, R. (2002) High-temperature experiments on silicate melt inclusions in olivine at 1 atm: inference on temperatures of homogenization and H_2O concentrations. Chemical Geology, 183, 87-98.

Métrich, N. and Wallace, P.J. (2008) Volatile abundances in basaltic magmas and their degassing paths tracked by melt inclusions. Reviews in Mineralogy & Geochemistry, 69, 363-402.

Newman, S. and Lowenstern, J.B. (2002) VolatileCalc: a silicate melt–H_2O–CO_2 solution model written in Visual Basic for excel. Computers & Geosciences, 28, 597-604.

Ochs III, F.A., Lange, R.A. (1997) The partial molar volume, thermal expansivity, and compressibility of H_2O in $NaAlSi_3O_8$ liquid: new measurements and an internally-consistent model. Contributions to Mineralogy and Petrology, 129, 155-165

Papale, P., Moretti, R., and Barbato, D. (2006) The compositional dependence of the saturation surface of H2O + CO2 fluids in silicate melts. Chemical Geology, 229, 78-95.

Pichavant, M., Carlo, I.D., Rotolo, S.G., Scaullet, B., Burgisser, A., Le Gall, N., and Martel, C. (2013) Generation of CO2-rich melts during basalt magma ascent and degassing. Contributions to Mineralogy and Petrology, 166, 545–561.

Rapien, M.H., Bodnar, R.J., Simmons, S., Szabó, Cs., Wood, C.P., and Sutton, S.R. (2003) Melt inclusion study of the embryonic porphyry copper system at White Island, New Zealand. Society of Economic Geologists Special Publication 10, 41-59.

Richter, D.H., Eaton, J.P., Murata, K.J., Ault, W.U., and Krivoy, H.L. (1970) Chronological narrative of the 1959-60 eruption of Kilauea Volcano, Hawaii. U.S. Geological Survey Professional Paper 537-E, 73 p.

Riker, J.M. (2005) The 1859 Eruption of Mauna Loa Volacano, Hawai'i: Controls on the Development of Long Lava Channels, 175 p. M.S. thesis, University of Oregon.

Roedder, E. (1979) Origin and significance of magmatic inclusions. Bulletin de Mineralogie, 102, 467-510.

Roedder, E. (1984) Fluid Inclusions. Mineralogical Society of America, Reviews in Mineralogy, v. 12, 644 p.

Roggensack, K. (2001) Unraveling the 1974 eruption of Fuego volcano (Guatemala) with small crystals and their young melt inclusions. Geology, 29, 10, 911-914.

Roggensack, K., Hervig, R.L., McKnight, S.B., and Williams, S.N. (1997) Explosive Basaltic Volcanism from Cerro Negro Volcano: Influence of Volatiles on Eruptive Style. Science, 227, 5332, 1639-1642.

Rose, W.I., Anderson, A.T., Woodruff, L.G., and Bonis, S.B. (1978) The October 1974 basaltic tephra from Fuego Volcano: Description and history of the magma body. Journal of Volcanology and Geothermal Research, 4, 3-53.

Ruscitto, D.M., Wallace, P.J., Johnson, E.R., Kent, A.J.R., and Bindeman, I.N. (2010) Volatile contents of mafic magmas from cinder cones in the Central Oregon High Cascades: Implications for magma formation and mantle conditions in a hot arc. Earth and Planetary Science Letters, 298, 153–161.

Schipper, C.I., White, J.D.L., Houghton, B.F., Shimizu, N., and Stewart, R.B. (2010) Explosive submarine eruptions driven by volatile-coupled degassing at Loihi Seamount, Hawaii. Earth and Planetary Science Letters, 295, 497-510.

Severs, M.J., Azbej, T., Thomas, J.B., Mandeville, C.W., and Bodnar, R.J. (2007) Experimental determination of H_2O loss from melt inclusions during laboratory heating: Evidence from Raman spectroscopy. Chemical Geology, 237, 358-371.

Severs, M.J., Beard, J.S., Fedele, L., Hanchar, J.M., Muchler, S.R., and Bodnar, R.J. (2009) Partitioning behavior of trace elements between dacitic melt and plagioclase, orthopyroxene, and clinopyroxene based on laser ablation ICPMS analysis of silicate melt inclusions. Geochimica et Cosmochimica Acta, 73, 2123–2141.

Shaw, A.M., Hauri, E.H., Fischer, T.P., Hilton, D.R., and Kelly, K.A. (2008) Hydrogen isotopes in Mariana arc melt inclusions: Implications for subduction dehydration and the deep-Earth water cycle. Earth and Planetary Science Letters, 275, 138–145.

Skirius, C.M., Peterson, J.W, and Anderson, A.T., Jr. (1990) Homogenizing rhyolitic glass inclusions from the Bishop Tuff. American Mineralalogist 75, 1381-1398.

Smith, C.L., Sykes, D., Almeida, N., and Ahmed, F. (2013) X-ray microtomography of Martian meteorites – current and future research/curation applications. Meteoritics and Planetary Science Supplement, 5323.

Sparks, R.S.J. (1978) The dynamics of bubble formation and growth in magmas: a review and analysis. Journal of Volcanology and Geothermal Research, (3) 1-37.

Spera, F.J. (2000) Physical properties of magmas. *Encyclopedia of Volcanoes, Eds. Sigurdsson, H., Houghton, B., McNutt, S. R., Rymer, H., Stix, J.* Academic Press, 171-190.

Spilliaert, N., Allard, P., Métrich, N., and Sobolev, A.V. (2006) Melt inclusion record of the conditions of ascent, degassing, and extrusion of volatile-rich alkali basalt during the powerful 2002 flank eruption of Mount Etna (Italy). Journal of Geophysical Research, 111, 19 p.

Steele-MacInnis, M., Esposito, R., and Bodnar, R.J., (2011) Thermodynamic model for the effect of post-entrapment crystallization on the H_2O-CO_2 systematics of vapor-saturated, silicate melt inclusions. Journal of Petrology, 52, 2461-2482.

Sterner, S.M. and Bodnar, R.J. (1984) Synthetic fluid inclusions in natural quartz I. Compositional types synthesized and applications to experimental geochemistry. Geochimica et Cosmochimica Acta, 48, 2659–2668.

Stolper, E. and Holloway, J.R. (1988) Experimental determination of the solubility of carbon dioxide in molten basalt at low pressure. Earth and Planetary Science Letters, 87, 397-408.

Student, J.J., and Bodnar, R.J. (2004) Silicate melt inclusions in porphyry copper deposits: Identification and homogenization behavior. Canadian Mineralogist, **42**,1583-1599.

Thomas, J.B. and Bodnar, R.J. (2002) A technique for mounting and polishing melt inclusions in small (<1 mm) crystals. American Mineralogist, 87, 1505–1508.

Tilling, R.I. and Dvorak, J.J. (1993) Anatomy of a basaltic volcano. Nature, 363, 125-133.

Tuohy, R. (2013) Olivine crystallization depths within Kilauea's lower east rift zone: The use of rehomogenized melt inclusions to interpret magma transport, storage and energetic fountaining. M.S. thesis, University of Oregon.

Vigouroux, N., Wallace, P.J., and Kent, A.J.R. (2008) Volatiles in high-K magmas from the western Trans-Mexican Volcanic Belt: Evidence for fluid fluxing and extreme enrichment of the mantle wedge by subduction processes. Journal of Petrology, 49 (9), 1589-1618.

Walker, J.A. (2003) The water and trace element contents of melt inclusions across an active subduction zone. Contributions to Mineralogy and Petrology, 146, 62-77.

Wallace, P.J. (2005) Volatiles in subduction zone magmas: concentrations and fluxes based on melt inclusion and volcanic gas data. Journal of Volcanology and Geothermal Research, 140, 217-240.

Wallace, P.J., Anderson, A.T., and Davis, A.M. (1999) Gradients in H2O, CO2, and exsolved gas in a large-volume silicic magma system: Interpreting the record preserved in melt inclusions from the Bishop Tuff. Journal of Geophysical Research, 104, B9, 20,097 - 20,122.

Wallace, P.J. and Gerlach, T.M. (1994) Magmatic Vapor Source for Sulfur Dioxide Released During Volcanic Eruptions: Evidence from Mount Pinatubo. Science, 265, 497-499.

Wallace, P.J., Kamenetsky, V.S. and Cervantes, P. (in review) Inclusion CO_2 contents, pressures of olivine crystallization, and the problem of shrinkage bubbles. American Mineralogist, in review.

Watson, E.B., Sneeringer, M.A., and Ross, A. (1982) Diffusion of dissolved carbonate in magmas: experimental results and applications. Earth and Planetary Science Letters, 61, 346-358.

Webb, S. (1997) Silicate melts: relaxation, rheology, and the glass transition. Reviews of Geophysics, 35, 2, 191-218.

Webster, J.D., Raia, F., De Vivo, B., and Rolandi, G. (2001) The behavior of chlorine and sulfur during differentiation of the Mt. Somma-Vesuvius magmatic system. Mineralogy & Petrology, 73, 177-200.

Yang, K. and Bodnar, R.J. (1994) Magmatic-hydrothermal evolution in the “bottoms” of porphyry copper systems: Evidence from silicate melt and aqueous inclusions in granitoid intrusions in the Gyeongsang Basin, South Korea. International Geology Review, **36**, 608-628.

Zimmer, M.M., Plank, T., Hauri, E.H., Yogodzinski, G.M., Stelling, P., Larsen, J., Singer, B., Jicha, B., Mandeville, C., and Nye, C.J. (2010) The role of water in generating the calc-alkaline trend: New volatile data for Aleutian magmas and a new tholeiitic index. Journal of Petrology, 51(12), 2411-2444.

Zhang, Y., Xu, Z., Zhu, M., and Wang, H. (2007) Silicate melt properties and volcanic eruptions. Reviews of Geophysics, 45, 27 p.

FIGURE CAPTIONS

Figure 1. A pseudo-degassing path represented by a group of MI that all trapped a melt containing 1200 ppm CO_2, but lost varying amounts of CO_2 to the bubble after trapping. The symbols represent the CO_2 content of the glass phase in MI that formed vapor bubbles of various sizes (0.5-2.0 volume percent; symbol size is proportional to volume percent vapor) and densities (indicated by different symbol shapes; 0.04-0.16 g/cm^3). Isobars represent solubility relationships for a basaltic melt predicted using VolatileCalc (Newman and Lowenstern, 2002). The pseudo-degassing path is indistinguishable from a true degassing path.

Figure 2. Raman spectrum of a vapor bubble in an olivine-hosted MI from the 1974 eruption of Fuego volcano (Table 3, Fuego 19.1). Peaks corresponding to the olivine host crystal (olivine doublet) and CO_2 in the bubble (the Fermi diad) are labeled. The density of CO_2 in the bubble is related to the distance between the two peaks in the Fermi diad (Δ, cm^{-1}), and was calculated using the equation of Fall et al. (2011).

Figure 3. Photomicrographs of representative MI from this study. (a) a typical glassy MI (Kil Iki Nat R 3_10) hosted in olivine from tephra erupted by Kilauea Iki (1959 eruption) shown in transmitted light. (b) a typical glassy MI (Kap 8 Nat R 5_3) in olivine from tephra erupted by Kapoho (1960 eruption) shown in transmitted light. Some of the MI from Kilauea Iki and Kapoho contain opaque daughter spinels (?) as shown in (b). (c) MI from the 1974 eruption of Fuego Volcano, Guatemala that contains a spinel (?) daughter mineral and a single vapor bubble (Table 3, Fuego MI 11.1) (d) a typical glassy, bubble-bearing MI (Seguam 14.1) hosted by olivine from tephras erupted on Pyre Peak (1977), Seguam Island, Alaska. This MI shows the

"wrinkled" texture that is common in the larger MI (~100 µm or larger) from these samples. (e) An olivine-hosted MI from Seguam Island, Alaska (SEG 7.1) that contains carbonate daughter minerals that have formed at the bubble-glass interface shown in transmitted light. (f) a photomicrograph of the bubble from (e) in reflected light; the image contrast is enhanced for greater visibility of carbonate minerals. Carbonate was detected during Raman analysis of the bubble, and the bright texture visible in reflected light is due to the scattering of light from the crystal faces of the carbonate minerals. The carbonate daughter minerals could contain a significant amount of C that would not be accounted for based on Raman analysis of CO_2 in the vapor bubble ± the glass in our study (see text).

Figure 4. Relationship between MI volume and vapor bubble volume with contours of volume percent vapor for (a) bubble-bearing MI in two phenocrysts from Kilauea Iki, and (b) all bubble-bearing MI from Seguam and Fuego (see text). A linear relationship between MI volume and vapor bubble volume indicates that all MI contain the same volume proportion of vapor, and this suggests that the MI trapped only melt and that the bubbles were generated in the MI after trapping. One of the phenocrysts from Kilauea (Kil Iki Nat R 4) hosts a melt inclusion assemblage (MIA) with a more random relationship between MI and vapor bubble volumes, especially for the smaller MI. This suggests that some of the MI in this phenocryst may have trapped a mixture of melt and vapor. For this reason, none of the MI from this phenocryst were used to estimate the total amount of CO_2 in the MI (see text). Vapor bubble volumes were calculated by measuring the bubble diameters and assuming that they are spheres. Most MI have shapes that are approximated as oblate spheres, and the volumes were calculated using the measured long and short dimensions of the oblate sphere (see text).

Figure 5. H_2O and CO_2 contents of MI from a) the 1959 Iki eruption at the summit of Kilauea (Hawaii), b) the 1960 Kapoho eruption on the East Rift Zone of Kilauea, c) the 1974 eruption of Fuego volcano (Guatemala), and d) the 1977 eruption of Seguam Island (Alaska). (a-d) on the left side of each figure is a histogram of minimum concentrations of CO_2 in the melt calculated by Raman analysis of MI vapor bubbles only and assuming that the glass contains no CO_2 (see text). On the right side of each figure are H_2O and CO_2 concentrations that include both measurements of the glass and vapor portions of the MI. Isobars were calculated with VolatileCalc (Newman & Lowenstern, 2002). Open symbols indicate volatile contents determined by analyzing the glass. Filled symbols indicate reconstructed melt compositions calculated after Raman analysis of the vapor bubble (see text, Table 5). Crosses indicate volatile contents in the glass in the MI for which CO_2 could not be quantified in the bubble. CO_2 in the vapor bubble was quantified using Raman spectroscopy. a-b) Volatile contents in the glass were determined by FTIR (Tuohy et al., in preparation). c-d) Volatile contents in the glass were determined by SIMS at CIW. Dashed and shaded fields delineate MI glass compositions analyzed in other studies of MI from the same four eruptions. Note that the histograms on the left include all MI for which Raman analyses of the vapor bubbles were available, whereas the data on the right are for those MI for which the CO_2 content of the glass is available from FTIR or SIMS analysis. Moreover, analyses of the vapor bubbles are available for some of the MI shown on the right diagrams, and these MI are therefore also included in the histograms, ignoring the known CO_2 content of the glass (i.e., the CO_2 content of the glass is assumed to be zero).

Figure 6. Relationship between the density of CO_2 measured in the vapor bubbles of glassy MI and the volume proportion of vapor in MI from a) the 1959 Iki eruption at the summit of Kilauea (Hawaii) and the 1960 Kapoho eruption on the East Rift Zone of Kilauea, b) the 1974 eruption of Fuego volcano (Guatemala), and c) the 1977 Pyre Peak eruption of Seguam Island (Alaska). The contours show the proportion of the total amount of CO_2 in the MI that is contained in the bubble, assuming a bulk glass density of 2.75 g/cm^3 and CO_2 concentrations in the glass of 300 ppm CO_2 (a), 700 ppm CO_2 (b), and 500 CO_2 (c). These values represent the highest concentrations reported in the literature for MI from Kilauea, Fuego, and Seguam, respectively (Anderson & Brown, 1993; Lloyd et al., 2013; Zimmer et al., 2010; see text, Figure 5 caption). This combination of Raman and petrographic analysis suggests that ~2 to 90 percent of the total CO_2 in the MI is contained in the vapor bubble (Tables 2, 3, 4). These predictions were confirmed by analyses of the MI glass (Table 5). The contours shown in d) show the relationship between the proportion the total CO_2 in the MI that is contained in the vapor bubble the CO_2 concentration of the glass, for CO_2 densities of 0.001 and 0.1 g/cm^3 and for vapor bubbles occupying 0.1, 1 and 10 volume percent of the MI.

Figure 7. A comparison of predicted and measured proportion of the total CO_2 in the MI that is contained in the vapor bubble. a) The Y-axis shows the calculated mass percent of CO_2 in the MI that is contained in the vapor bubble for MI in which the CO_2 content of the glass is known from SIMS and/or FTIR analyses and the amount of CO_2 in the vapor bubble is known from Raman analyses. The X-axis shows the mass percent of CO_2 in the MI that is contained in the vapor that was calculated using only data for CO_2 in the vapor bubble obtained by Raman analyses combined with the maximum reported CO_2 contents (ignoring outliers) of the glass phase in MI

from these same eruptions from the literature. b-d) the distribution of measured CO_2 concentrations of the glass phase in MI from Kilauea, Fuego, and Seguam reported by Anderson and Brown (1993), Lloyd et al. (2013), and Zimmer et al., (2010), respectively. The dashed lines indicate the values used in this study to calculate the proportion of the total amount of CO_2 in the MI that is contained in the vapor bubble and shown on Figure 6.

Figure 8. Calculated change in volume of the melt and the host phase during cooling from the temperature of trapping to the glass transition temperature, for MI hosted in a) olivine, b) anorthite, c) orthopyroxene, d) clinopyroxene, e) alkali feldspar, and f) quartz. Volumetric properties of melts were calculated using thermodynamic data from Lange & Carmichael (1990), Lange (1997), and Ochs and Lange (1997). Volumetric properties of minerals were calculated from unit cell parameters experimentally determined over a range of temperatures. The sources for mineral and melt data are shown in the inset of each panel. Volumetric properties of melts and crystals are normalized to the volume of each at the temperature of trapping. Isopleths of vapor volume represent the difference between the change in melt volume and the change in the host phase volume during cooling. Vapor bubble volumes vary depending on the cooling interval (ΔT, e.g. Riker, 2005) experienced by the MI, and this, in turn, depends on the trapping temperature of the inclusion and the glass transition temperature of the melt.

Figure 9. A comparison of reconstructed CO_2 concentrations of MI estimated using the Ideal Gas Law (IGL), an empirically-derived equation of state (Mao EOS), and *in situ* Raman analysis of the bubble. a) Comparison of the reconstructed CO_2 concentration in the MI calculated with the IGL and the reconstructed CO_2 concentration in the MI calculated from the CO_2 density in

the vapor bubble estimated from Raman analysis. A 1-to-1 reference line is plotted as a solid line, and the dashed lines represent 1-to-3 (IGL concentration to Raman concentration) and 1-to-10 reference lines showing the extent to which the IGL overestimates the CO_2 contents of the MI. b) Comparison of the reconstructed CO_2 contents of the MI calculated with the IGL and those predicted using the Mao EOS to estimate the volumetric properties of the fluid phase in the vapor bubble. Both equations predict similar concentrations for the CO_2 contents of the MI in this study (see text).

Fig 1

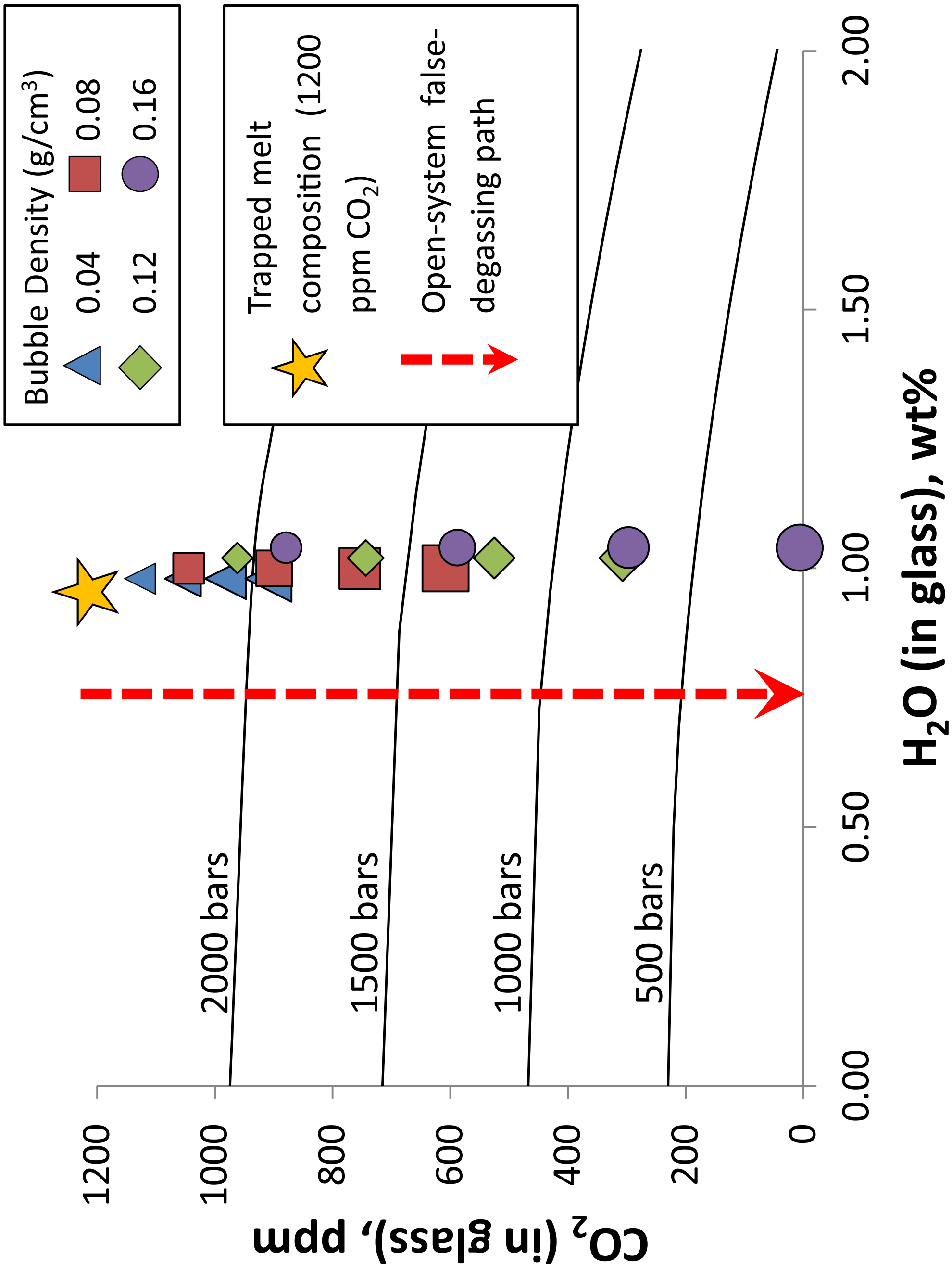
Bubble Density (g/cm^3)
▲ 0.04
■ 0.08
◆ 0.12
● 0.16
★ Trapped melt composition (1200 ppm CO_2)
Open-system false-degassing path
2000 bars
1500 bars
1000 bars
500 bars
CO_2 (in glass), ppm
1200
1000
800
600
400
200
0
H_2O (in glass), wt%
0.00
0.50
1.00
1.50
2.00

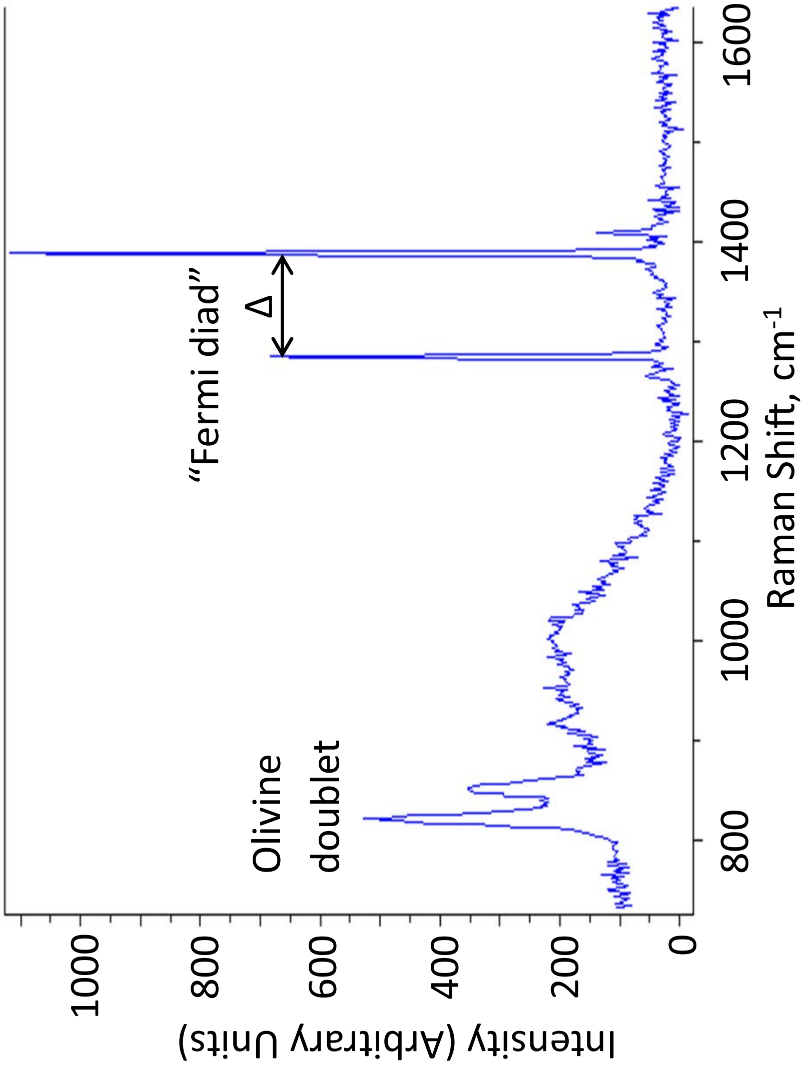
Olivine
doublet
"Fermi diad"
Δ
Intensity (Arbitrary Units)
0
200
400
600
800
1000
Raman Shift, cm^{-1}
800
1000
1200
1400
1600

Figure 2

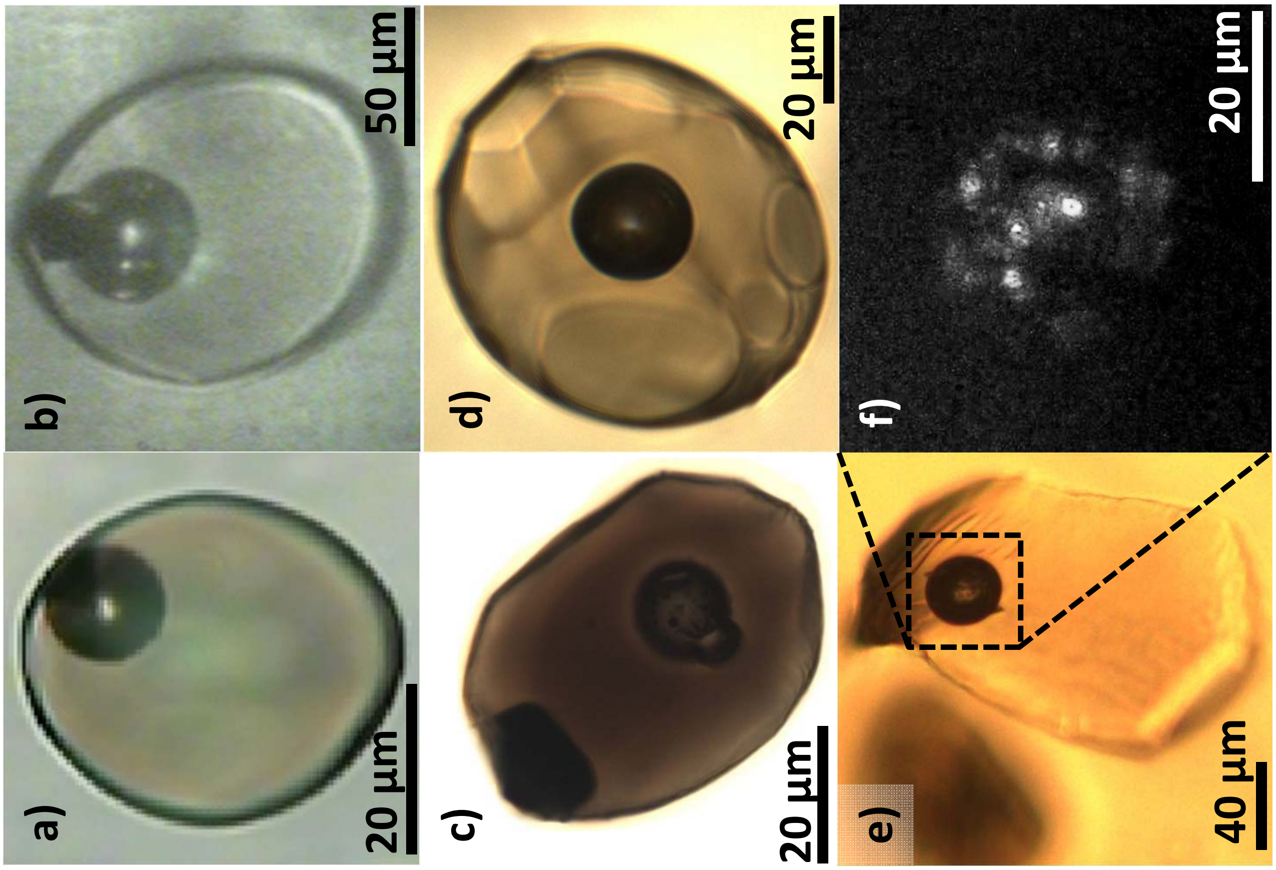

Figure 3

Fig 4

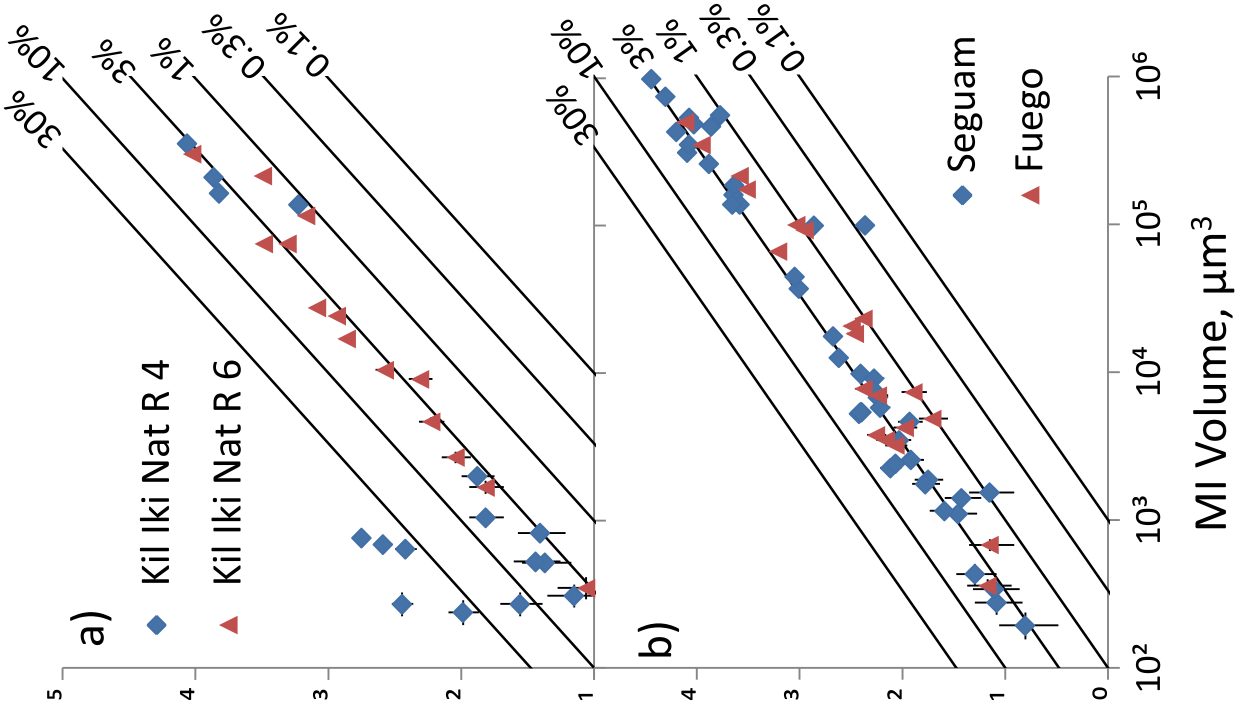
a)
◆ Kil Iki Nat R 4
▲ Kil Iki Nat R 6
b)
◆ Seguam
▲ Fuego
30%
10%
3%
1%
0.3%
0.1%
Bubble Volume, μm^3
10^5
10^4
10^3
10^2
10^1
10^0
MI Volume, μm^3
10^2
10^3
10^4
10^5
10^6

Figure 5

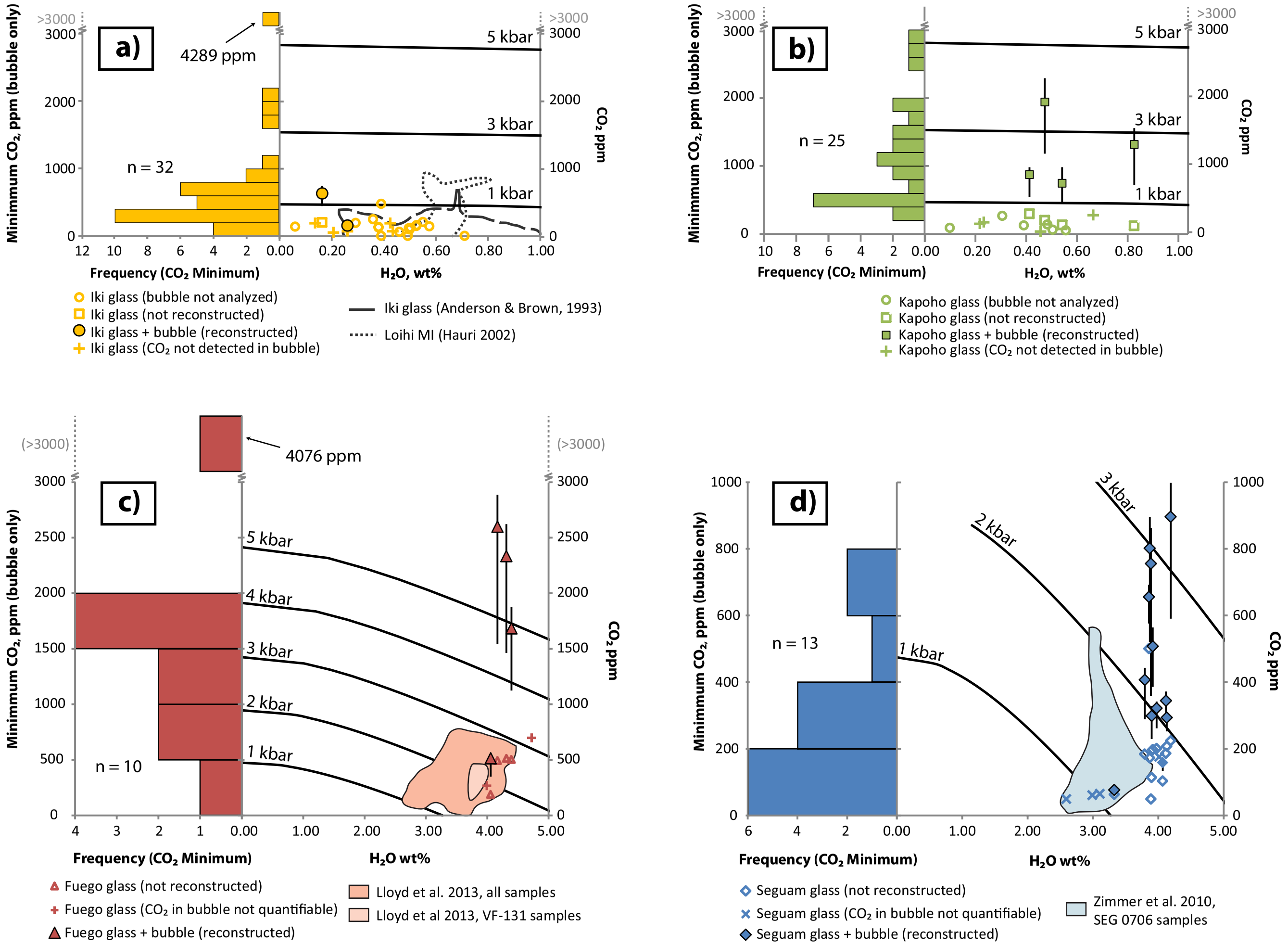
a)
>3000
3000
2000
1000
0
Minimmum CO₂, ppm (bubble only)
4289 ppm
n = 32
5 kbar
3 kbar
1 kbar
CO₂ ppm
12 10 8 6 4 2 0.00 0.20 0.40 0.60 0.80 1.00
Frequency (CO₂ Minimum)
H₂O, wt%
Iki glass (bubble not analyzed)
Iki glass (not reconstructed)
Iki glass + bubble (reconstructed)
Iki glass (CO₂ not detected in bubble)
Iki glass (Anderson & Brown, 1993)
Loihi MI (Hauri 2002)
b)
n = 25
10 8 6 4 2 0.00 0.20 0.40 0.60 0.80 1.00
Kapoho glass (bubble not analyzed)
Kapoho glass (not reconstructed)
Kapoho glass + bubble (reconstructed)
Kapoho glass (CO₂ not detected in bubble)
c)
(>3000)
2500
1500
500
4076 ppm
n = 10
4 kbar
2 kbar
4 3 2 1 0.00 1.00 2.00 3.00 4.00 5.00
H₂O wt%
Fuego glass (not reconstructed)
Fuego glass (CO₂ in bubble not quantifiable)
Fuego glass + bubble (reconstructed)
Lloyd et al. 2013, all samples
Lloyd et al 2013, VF-131 samples
d)
1000
800
600
400
200
n = 13
6 4 2 0.00 1.00 2.00 3.00 4.00 5.00
Seguam glass (not reconstructed)
Seguam glass (CO₂ in bubble not quantifiable)
Seguam glass + bubble (reconstructed)
Zimmer et al. 2010, SEG 0706 samples

Figure 6

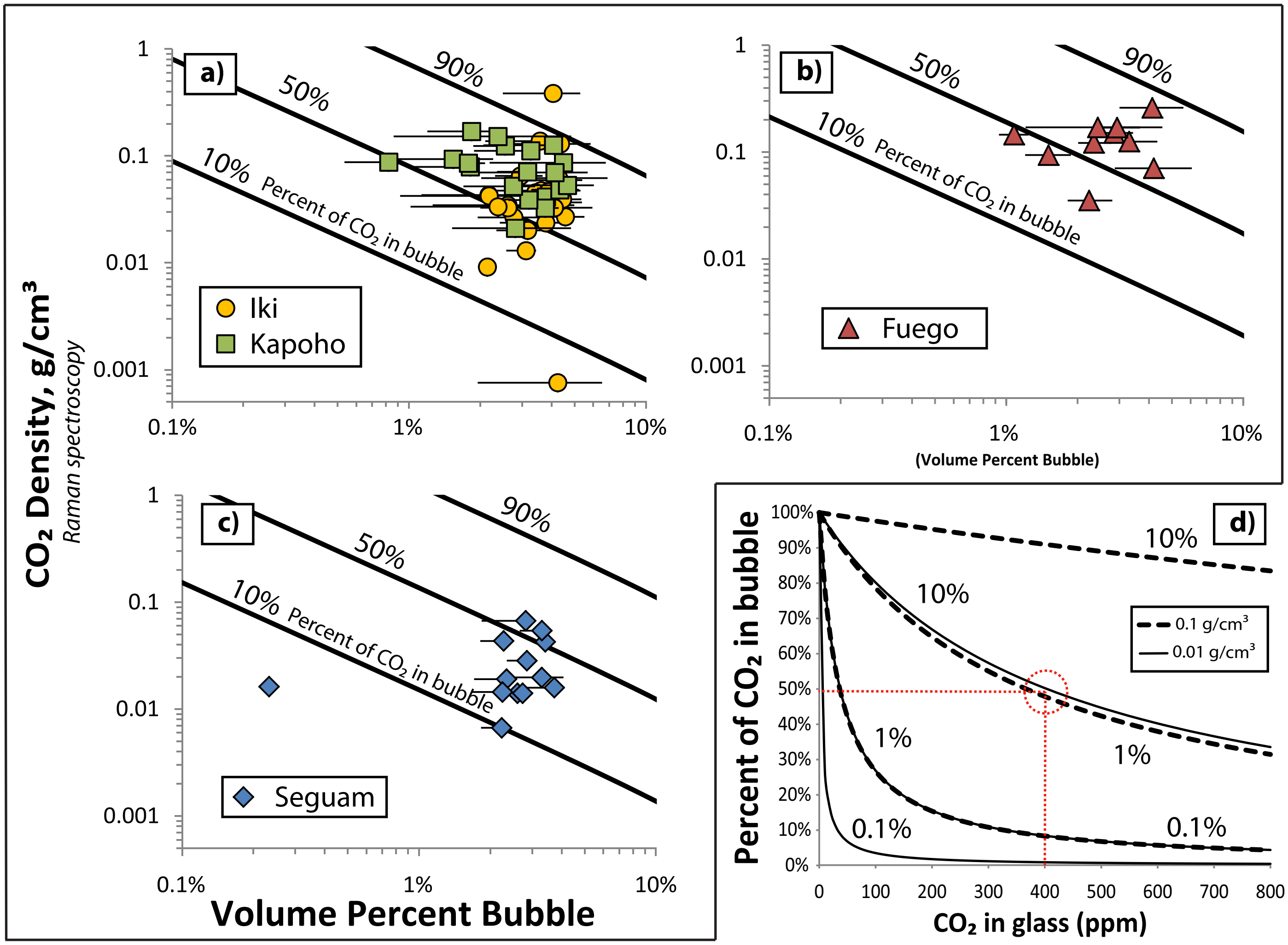
a)
90%
50%
10% Percent of CO_2 in bubble
Iki
Kapoho
1
0.1
0.01
0.001
0.1%
1%
10%
b)
90%
50%
10% Percent of CO_2 in bubble
Fuego
(Volume Percent Bubble)
CO_2 Density, g/cm³
Raman spectroscopy
c)
90%
50%
10% Percent of CO_2 in bubble
Seguam
Volume Percent Bubble
d)
Percent of CO_2 in bubble
100%
90%
80%
70%
60%
50%
40%
30%
20%
10%
0%
10%
10%
1%
1%
0.1%
0.1%
0.1 g/cm³
0.01 g/cm³
0
100
200
300
400
500
600
700
800
CO_2 in glass (ppm)

Figure 7

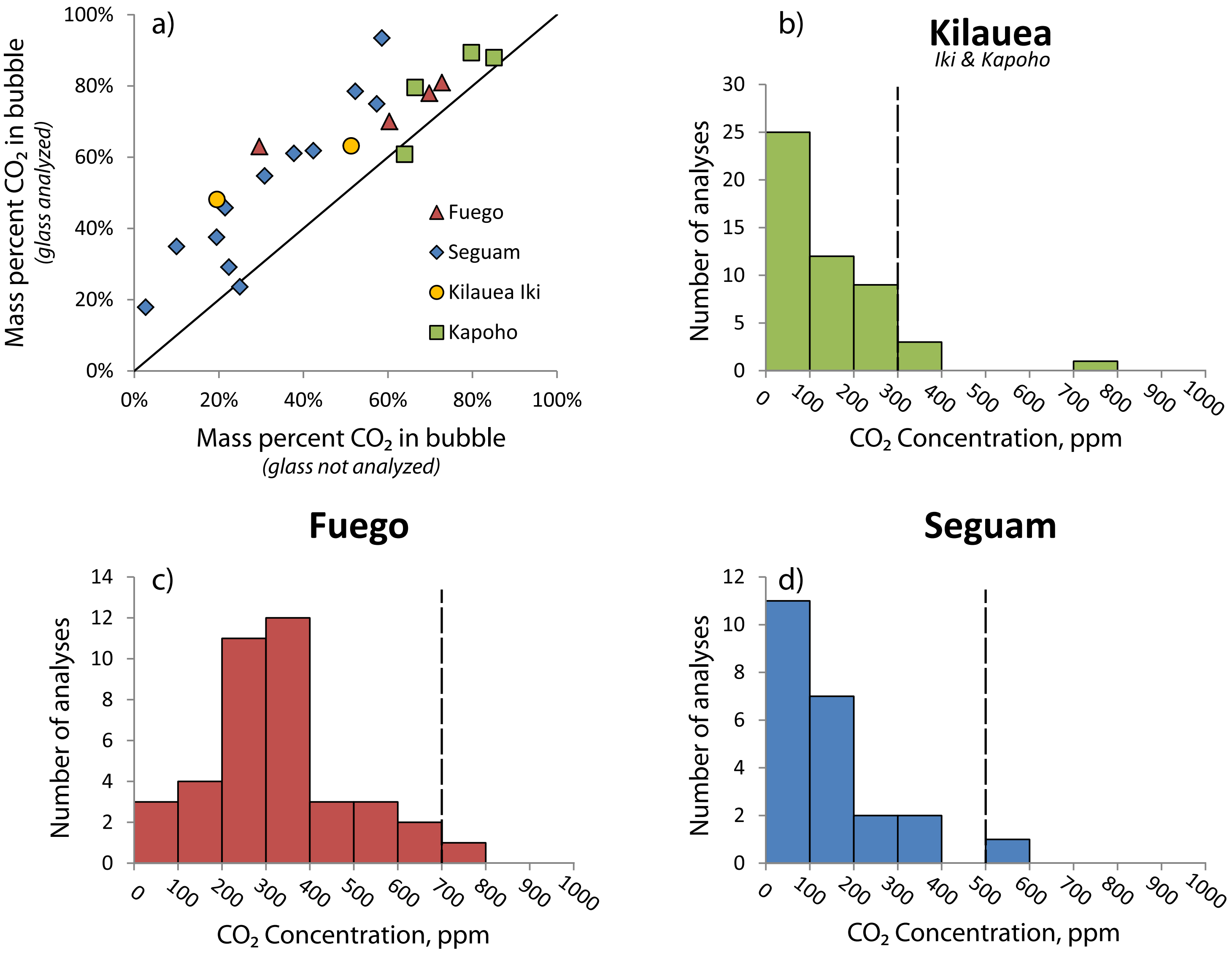
a)
Mass percent CO₂ in bubble
(glass analyzed)
Mass percent CO₂ in bubble
(glass not analyzed)
0%
20%
40%
60%
80%
100%
▲ Fuego
◆ Seguam
● Kilauea Iki
■ Kapoho
b)
Kilauea
Iki & Kapoho
Number of analyses
0
5
10
15
20
25
30
CO₂ Concentration, ppm
0
100
200
300
400
500
600
700
800
900
1000
Fuego
c)
Number of analyses
0
2
4
6
8
10
12
14
CO₂ Concentration, ppm
Seguam
d)
Number of analyses
0
2
4
6
8
10
12
CO₂ Concentration, ppm

Figure 8

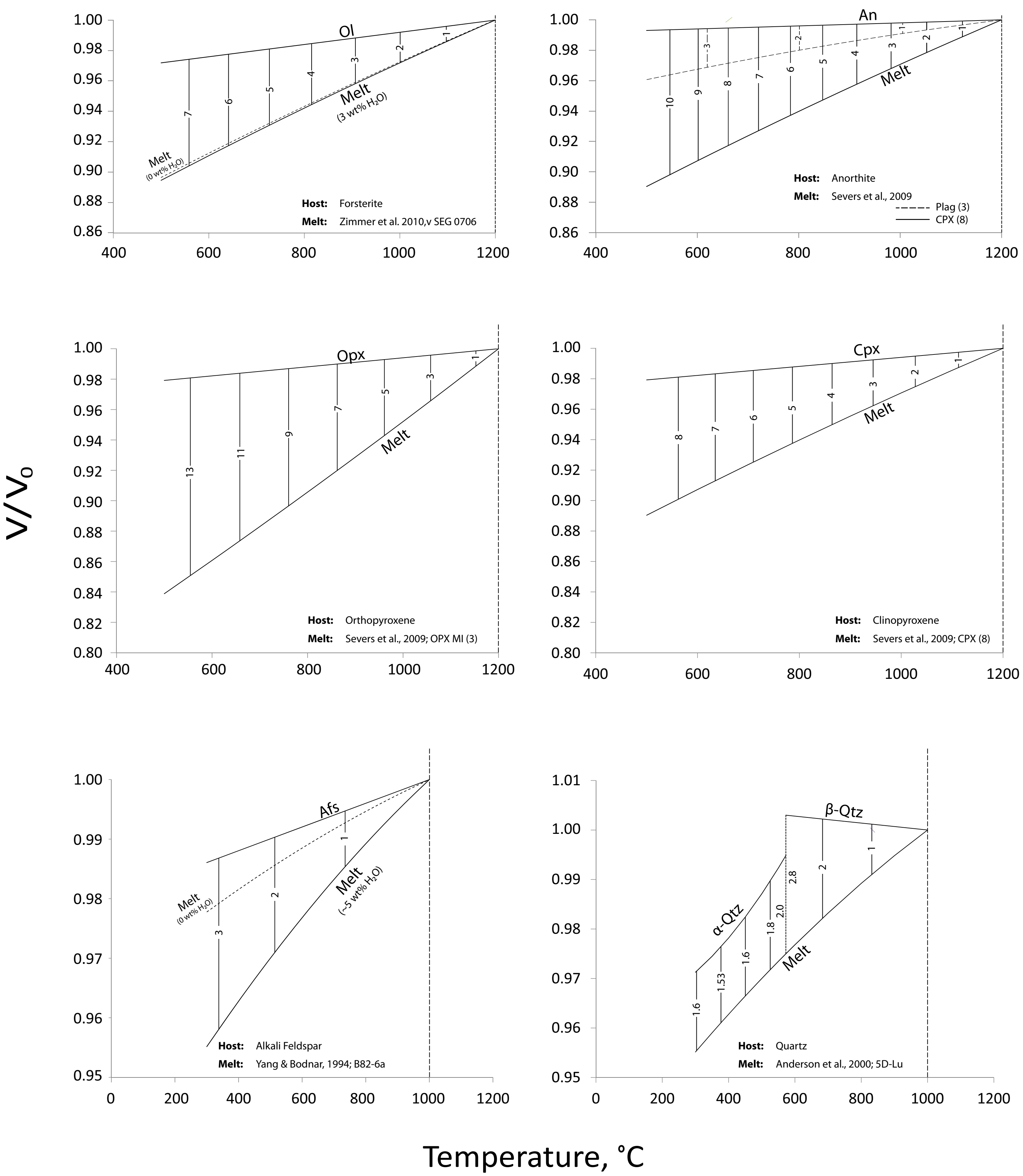
1.00
0.98
0.96
0.94
0.92
0.90
0.88
0.86
400
600
800
1000
1200
Ol
Melt
(3 wt% H$_2$O)
Melt
(0 wt% H$_2$O)
7
6
5
4
3
2
1
Host: Forsterite
Melt: Zimmer et al. 2010,v SEG 0706
An
Melt
10
9
8
7
6
5
4
3
2
1
Host: Anorthite
Melt: Severs et al., 2009
Plag (3)
CPX (8)
0.84
0.82
0.80
Opx
Melt
13
11
9
7
5
3
1
Host: Orthopyroxene
Melt: Severs et al., 2009; OPX MI (3)
Cpx
Melt
8
7
6
5
4
3
2
1
Host: Clinopyroxene
Melt: Severs et al., 2009; CPX (8)
V/V$_0$
0.99
0.97
0.95
0
200
Afs
Melt
(0 wt% H$_2$O)
Melt
(~5 wt% H$_2$O)
3
2
1
Host: Alkali Feldspar
Melt: Yang & Bodnar, 1994; B82-6a
1.01
β-Qtz
α-Qtz
Melt
1.6
1.53
1.6
1.8
2.0
2.8
2
1
Host: Quartz
Melt: Anderson et al., 2000; 5D-Lu
Temperature, °C

Figure 9

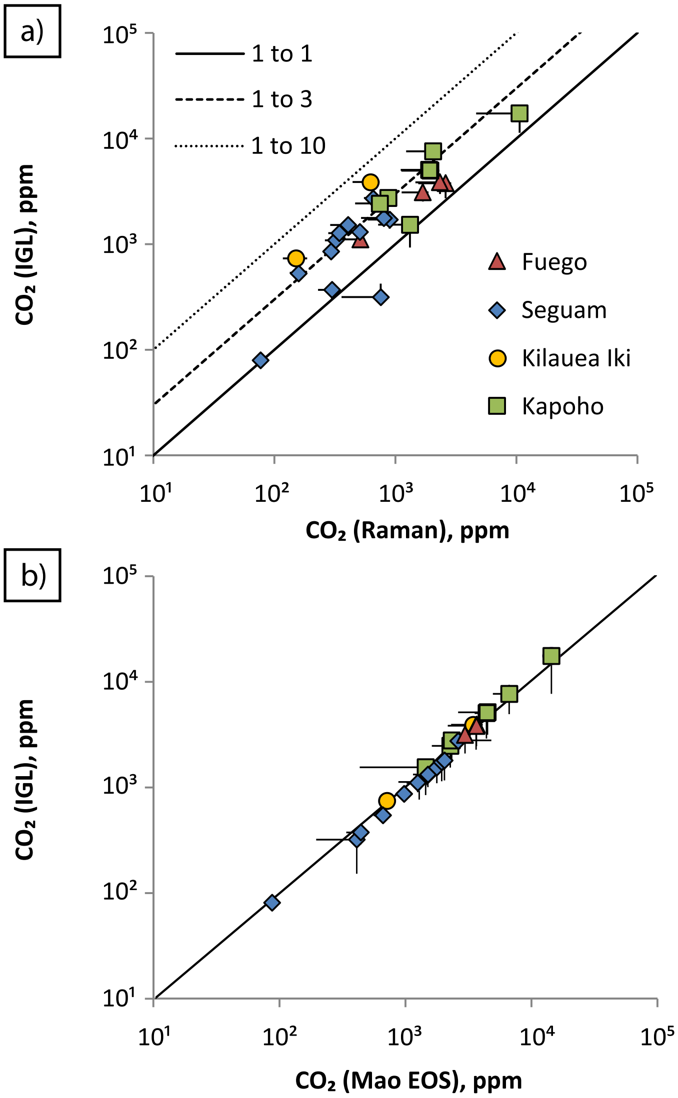
a)
1 to 1
1 to 3
1 to 10
Fuego
Seguam
Kilauea Iki
Kapoho
10^1
10^2
10^3
10^4
10^5
CO_2 (IGL), ppm
CO_2 (Raman), ppm
b)
CO_2 (IGL), ppm
CO_2 (Mao EOS), ppm

Table 1: Sources of MI data

Data Type	**Kilauea Iki**	**Kapoho**	**Fuego**	**Seguam**
CO_2 density in bubble[a]	Raman	Raman	Raman	Raman
Volatile concentrations in glass[b]	FTIR	FTIR	SIMS	SIMS
Major elements[c]	EPMA	EPMA	EPMA	EPMA
PEC correction[d]	Tuohy et al.	Tuohy et al.	petrolog3	Petrolog3

[a] Density of CO_2 in the bubble was determined for all eruptions by Raman analysis at Virginia Tech (VT). Samples for which we have analyzed vapor bubbles only and not the composition of the glass are indicated in Tables 2-4.

[b] Volatile concentrations in the glass were measured by FTIR at the University of Oregon (UO) by Tuohy et al. (in preparation) or by SIMS at the Carnegie Institution of Washington (CIW) as indicated.

[c] Major element concentrations of the glass were measured by EPMA. The MI from Kilauea Iki and Kapoho eruptions were analyzed at the University of Oregon by Tuohy et al. (in preparation). The MI from Fuego and Seguam eruptions were analyzed at Virginia Tech.

[d] All MI major element and volatile concentrations in this study have been corrected for PEC either by Tuohy et al. (in preparation) or using Petrolog3 software as indicated.

Table 2: Petrographic and Raman data for MI from Kilauea iki and Kapoho.

Sample	MI Number[a]	Peak 1, cm^{-1} [b]	Peak 2, cm^{-1} [b]	Δ, cm^{-1}	CO$_2$ density, g/cm^3 [c]	MI long diameter, µm	MI short diameter, µm	Bubble diameter, µm	Volume percent bubble[d]	Daughter minerals[e]	CO$_2$ min[f]	Percent of total CO$_2$ contained in the bubble[g]
Kil Iki Nat R	1_1	1284.78	1387.52	102.74	0.03	20	17	7	7%			
Kil Iki Nat R	1_2	1284.72	1387.53	102.81	0.06	24	23	8	4%		948	76%
Kil Iki Nat R	1_3	1284.93	1387.59	102.66	0.01	14	12	5	6%			
Kil Iki Nat R	1_4	d	d			12	12	4	4%			
Kil Iki Nat R	1_5	d	d			16	15	8	13%	s		
Kil Iki Nat R	1_6	1284.82	1387.54	102.72	0.03	32	29	11	5%		469	61%
Kil Iki Nat R	1_7	1284.78	1387.59	102.80	0.06	22	20	9	8%	s		
Kil Iki Nat R	1_8	d	d			13	12	5	5%			
Kil Iki Nat R	1_9	1284.16	1387.15	102.98	0.13	37	37	26	34%	s		
Kil Iki Nat R	1_10	1284.80	1387.57	102.77	0.04	57	55	18	4%	s	601	67%
Kil Iki Nat R	1_11	1284.87	1387.60	102.74	0.03	38	37	14	6%	s		
Kil Iki Nat R	1_12	1284.93	1387.62	102.69	0.02	15	15	6	6%	s		
Kil Iki Nat R	1_13	1286.62	1389.58	102.96	0.12	9	9	4	7%			
Kil Iki Nat R	2_1	1285.40	1388.12	102.72	0.03	19	19	6	3%		275	48%
Kil Iki Nat R	2_2	1285.35	1388.09	102.75	0.04	26	24	9	4%	s	595	66%
Kil Iki Nat R	2_3	1285.44	1388.18	102.74	0.03	10	10	3	3%	s	338	53%
Kil Iki Nat R	2_4	1285.46	1388.23	102.77	0.04	12	11	3	2%		347	54%
Kil Iki Nat R	2_5	1285.48	1388.21	102.74	0.03	27	26	8	3%	s	320	52%
Kil Iki Nat R	2_6	1285.55	1388.25	102.70	0.02	26	24	8	3%	s	240	44%
Kil Iki Nat R	2_7	1285.35	1388.18	102.83	0.07	29	29	9	3%	s	719	71%
Kil Iki Nat R	2_8	-	1388.38			17	16	5	3%	s		
Kil Iki Nat R	2_9	1285.53	1388.22	102.68	0.01	67	61	20	3%		152	34%
Kil Iki Nat R	2_10	1285.58	1388.33	102.76	0.04	49	48	16	3%	s	522	63%
Kil Iki Nat R	2_11	1285.59	1388.35	102.76	0.04	32	30	11	4%		666	69%
Kil Iki Nat R	2_12	-	-			60	57	19	4%			
Kil Iki Nat R	3_1w*	1285.72	1388.39	102.67	0.01	168	165	46	2%	s	73	20%
Kil Iki Nat R	3_2	1285.79	1388.44	102.65	0.00	16	12	5	4%		12	4%
Kil Iki Nat R	3_3	1285.64	1388.39	102.75	0.04	53	43	17	5%		707	70%
Kil Iki Nat R	3_4	1285.63	1388.34	102.71	0.02	41	31	11	4%	s	339	53%
Kil Iki Nat R	3_5	1285.70	1388.44	102.74	0.03	16	15	5	4%		510	63%

Kil Iki Nat R	3_6	1285.63	1388.44	102.82	0.06	14	11	4	4%	s	1008	77%
Kil Iki Nat R	3_7	1285.72	1388.49	102.78	0.05	17	14	5	4%	s	646	68%
Kil Iki Nat R	3_8	-	-			101	91	22	1%	s		
Kil Iki Nat R	3_9	1285.64	1388.41	102.77	0.05	58	50	17	3%		582	66%
Kil Iki Nat R	3_10	1284.11	1387.10	102.99	0.13	22	18	7	4%		2147	88%
Kil Iki Nat R	3_11	1285.74	1388.51	102.78	0.05	25	23	8	4%		679	69%
Kil Iki Nat R	3_12	1285.85	1388.61	102.76	0.04	17	12	4	2%	s	342	53%
Kil Iki Nat R	3_13	1285.87	1388.61	102.74	0.03	21	14	5	2%	s	296	50%
Kil Iki Nat R	3_14	1285.78	1388.55	102.77	0.04	24	24	9	5%	s	888	75%
Kil Iki Nat R	4_1	1283.96	1387.32	103.36	0.29	71	67	23	4%	s	4289	93%
Kil Iki Nat R	4_2	1284.24	1387.25	103.01	0.14	76	73	24	3%		1764	85%
Kil Iki Nat R	4_3	-	-			68	62	15	1%	s		
Kil Iki Nat R	4_4w*	1284.80	1387.52	102.72	0.03	94	86	28	3%	s	316	51%
Kil Iki Nat R	4_5	1283.82	1386.72	102.90	0.09	14	12	5	6%			
Kil Iki Nat R	4_6	1284.33	1387.02	102.69	0.02	12	11	9	56%			
Kil Iki Nat R	4_7	1283.44	1386.41	102.97	0.12	8	8	4	13%			
Kil Iki Nat R	4_8	1283.57	1386.59	103.02	0.14	11	11	8	41%	s		
Kil Iki Nat R	4_9	1286.67	1386.77	100.10	0.25	8	8	6	41%			
Kil Iki Nat R	4_10	1283.72	1386.74	103.02	0.14	8	8	8	99%			
Kil Iki Nat R	4_11	-	-			10	10	4	5%			
Kil Iki Nat R	4_12	-	-			16	16	5	4%			
Kil Iki Nat R	4_13	-	-			11	10	4	5%	s		
Kil Iki Nat R	4_14	-	-			10	8	3	5%			
Kil Iki Nat R	4_15	1283.87	1386.69	102.82	0.06	12	12	4	3%			
Kil Iki Nat R	4_16	1283.43	1386.54	103.11	0.18	12	11	10	74%			
Kil Iki Nat R	5_1	-	-			32	25	8	3%	s		
Kil Iki Nat R	5_2	-	-			71	65	19	2%			
Kil Iki Nat R	6_1	-	-			61	49	16	3%	s		
Kil Iki Nat R	6_2	d	d			42	35	13	4%			
Kil Iki Nat R	6_3	-	-			24	20	7	4%			
Kil Iki Nat R	6_4wb*	d	d			84	83	27	3%	s		
Kil Iki Nat R	6_5	-	-			31	24	7	2%	s		
Kil Iki Nat R	6_6	-	-			62	48	18	4%	s		
Kil Iki Nat R	6_7	1284.74	1387.39	102.65	0.00	96	66	18	1%		8	2%
Kil Iki Nat R	6_8	1284.86	1387.64	102.78	0.05	75	55	14	1%		222	43%

Kil Iki Nat R	6_9	-	-			10	8	3	3%			
Kil Iki Nat R	6_10	-	-			18	13	5	4%			
Kil Iki Nat R	6_11	1284.24	1387.25	103.01	0.14	33	25	9	4%		1853	86%
Kil Iki Nat R	6_12	-	1387.28			45	32	12	4%	s		
Kil Iki Nat R	6_13	-	1387.34			40	29	11	4%	s		
Kil Iki Nat R	6_14	-	-			23	15	6	4%			
Kil Iki Nat R	W1*	-	-			191	138	40	2%			
Kil Iki Nat R	W2*	-	-			257	215	59	2%			
Kil Iki Nat R	W5*	-	-			800	200	69	1%			
Kil Iki Nat R	W6a*	-	-			102	94	29	3%	s		
Kap 8 Nat R	1_1w*	1285.01	1387.99	102.98	0.12	333	250	81	3%		1177	80%
Kap 8 Nat R	1_2	-	-			48	46	13	2%			
Kap 8 Nat R	1_3	d	d			24	23	7	3%			
Kap 8 Nat R	2_1w*	d	d			394	245	101	4%			
Kap 8 Nat R	2_2	1284.51	1387.40	102.89	0.09	87	64	14	1%		263	47%
Kap 8 Nat R	2_3	1284.44	1387.30	102.87	0.08	77	77	31	6%			
Kap 8 Nat R	2_4	1284.47	1387.30	102.84	0.07	49	42	19	8%			
Kap 8 Nat R	2_5	1284.24	1387.26	103.02	0.14	9	8	3	6%			
Kap 8 Nat R	2_6	1284.37	1387.26	102.88	0.09	16	12	5	4%	s	1471	83%
Kap 8 Nat R	2_7	1284.07	1387.12	103.05	0.15	10	8	3	2%	c	1344	82%
Kap 8 Nat R	2_8	1285.10	1388.19	103.09	0.17	29	25	7	2%	s, c	1151	79%
Kap 8 Nat R	2_9	1284.21	1387.20	102.98	0.13	95	52	22	4%	s	1939	87%
Kap 8 Nat R	2_10	1284.15	1387.10	102.95	0.11	93	59	22	3%		1368	82%
Kap 8 Nat R	2_11	1284.43	1387.35	102.92	0.10	8	8	3	6%	s, c		
Kap 8 Nat R	2_12	1284.23	1387.22	102.98	0.13	9	8	3	7%	s, c		
Kap 8 Nat R	2_13	1284.20	1387.21	103.00	0.13	16	15	6	5%		2650	90%
Kap 8 Nat R	2_14	1284.29	1387.16	102.87	0.08	11	7	3	8%			
Kap 8 Nat R	2_15	1284.16	1387.07	102.91	0.10	8	7	3	8%			
Kap 8 Nat R	3_1w*	1285.74	1388.50	102.76	0.04	175	162	56	4%		592	66%
Kap 8 Nat R	3_2	1285.90	1388.63	102.74	0.03	46	45	15	4%		462	61%
Kap 8 Nat R	3_3	1285.86	1388.56	102.71	0.02	12	11	3	3%		222	42%
Kap 8 Nat R	3_4	d	d			12	12	4	4%			
Kap 8 Nat R	3_5	1285.12	1388.08	102.96	0.12	13	13	10	49%			
Kap 8 Nat R	3_6	1285.13	1388.09	102.96	0.12	17	17	16	87%			
Kap 8 Nat R	3_7	1285.99	1388.59	102.61	low	14	11	4	3%			

Kap 8 Nat R	3_8	1285.68	1388.44	102.76	0.04	79	70	23	3%		465	61%
Kap 8 Nat R	3_9	1285.16	1388.08	102.92	0.10	21	21	8	6%			
Kap 8 Nat R	3_10	1285.15	1388.07	102.92	0.10	23	23	9	6%			
Kap 8 Nat R	3_11	1285.16	1388.07	102.92	0.10	22	22	18	59%			
Kap 8 Nat R	3_12	-	-			21	21	6	3%	s		
Kap 8 Nat R	4_1w*	1284.72	1387.88	103.16	0.20	223	145	83	12%			
Kap 8 Nat R	4_2	-	-			13	11	5	10%			
Kap 8 Nat R	4_3	1284.91	1387.91	103.01	0.14	21	19	9	9%			
Kap 8 Nat R	4_4	1285.13	1388.00	102.87	0.08	47	29	13	6%			
Kap 8 Nat R	4_5	1285.42	1388.20	102.78	0.05	33	30	11	4%		793	73%
Kap 8 Nat R	4_6	1285.38	1388.17	102.79	0.05	25	20	8	5%	s	942	76%
Kap 8 Nat R	4_7	1285.27	1388.13	102.86	0.08	20	16	7	7%			
Kap 8 Nat R	4_8	1285.30	1388.16	102.86	0.08	20	16	6	5%	s	1524	84%
Kap 8 Nat R	4_9	1285.21	1388.20	103.00	0.13	18	16	7	8%			
Kap 8 Nat R	4_10	1285.20	1388.10	102.90	0.09	15	14	6	8%			
Kap 8 Nat R	4_11	1285.27	1388.13	102.86	0.08	12	12	5	8%			
Kap 8 Nat R	4_12	1285.21	1388.23	103.02	0.14	12	9	5	10%			
Kap 8 Nat R	5_1w*	-	-			122	109	37	4%	s		
Kap 8 Nat R	5_2w*	-	-			177	142	50	4%	s		
Kap 8 Nat R	5_3	1284.89	1387.80	102.91	0.10	47	42	17	7%	s		
Kap 8 Nat R	5_4	1284.33	1387.47	103.14	0.19	42	36	22	19%			
Kap 8 Nat R	5_5	1285.17	1387.96	102.79	0.05	36	28	9	3%	s	536	64%
Kap 8 Nat R	5_6	1284.92	1387.82	102.90	0.09	22	18	5	2%	s	529	64%
Kap 8 Nat R	5_7	1285.08	1387.91	102.84	0.07	25	15	6	4%	s	1093	78%
Kap 8 Nat R	5_8	1285.04	1387.95	102.91	0.10	17	14	6	5%	s	1929	87%
Kap 8 Nat R	5_9	1284.81	1387.78	102.97	0.12	12	12	5	8%			
Kap 8 Nat R	5_10	1284.85	1387.82	102.97	0.12	12	10	4	7%			
Kap 8 Nat R	5_11	1284.98	1387.91	102.93	0.10	9	7	4	10%			
Kap 8 Nat R	5_12	1285.00	1387.90	102.90	0.09	8	7	3	8%			
Kap 8 Nat R	6_1w*	1284.78	1387.64	102.86	0.08	501	296	93	2%		531	64%
Kap 8 Nat R	6_2	1284.76	1387.67	102.91	0.10	57	48	20	6%			
Kap 8 Nat R	6_3	1284.64	1387.58	102.94	0.11	93	61	31	9%			
Kap 8 Nat R	6_4	1284.78	1387.62	102.84	0.07	125	99	34	3%		844	74%
Kap 8 Nat R	6_5	1284.84	1387.72	102.88	0.09	45	44	12	2%		564	65%
Kap 8 Nat R	W2a*	-	-			201	129	61	7%			

Kap 8 Nat R	W3b*	d	d			343	275	87	3%			
Kap 8 Nat R	W5c*	-	-			166	124	56	7%	s		
Kap 8 Nat R	W7*	1284.80	1387.69	102.89	0.09	70	60	23	5%		1708	85%

[a] Samples for which the volatile content of the glass has been analyzed are indicated with an asterisk (*).

[b] Fermi diad peak positions determined by peak fitting of Raman spectra collected from MI (see methods) at Virginia Tech. Values marked as "-" indicate that CO_2 was not detected ; values marked as "d" indicate that CO_2 was detected, but the quality of the Raman spectra did not allow the peak splitting and thus CO_2 density to be quantified (see text).

[c] values marked as "low" indicate that the density could not be quantified with the Fall et al. (2011) equation for the measured peak separation (see text).

[d] The ratio of the volume of the bubble to the total MI volume was calculated by treating the bubble as a sphere and the MI as an oblate spheroid (see text).

[e] MI contain a chromite spinel (?)("s") or carbonates ("c") in addition to a bubble as indicated (see text).

[f] The minimum amount of CO_2 in the MI. This is calculated by Raman analysis of the bubble and by using a value of 0 ppm for the CO_2 contained in the glass.

[g] Percent of the total CO_2 in the MI that is contained in the bubble assuming a melt (glass) that contains 300 ppm CO_2 (see text)

Table 3: Petrographic and Raman data for MI from Fuego.

Sample	MI Number[a]	Peak 1, cm^{-1} [b]	Peak 2, cm^{-1} [b]	Δ, cm^{-1}	CO_2 density, g/cm^3 [c]	long diameter MI, µm[d]	short diameter MI, µm[d]	Bubble diameter, µm[d]	Volume percent bubble	daughter minerals[e]	CO_2 min[f]
Fuego	5.1	1285.28	1388.58	103.30	0.26	19	19	7	4%		4076
Fuego	5.2	-	-			24	n.r.	7	2%	s	
Fuego	5.3*	1285.18	1387.92	102.75	0.04	56	47	15	2%	s, c	293
Fuego	6.1	1286.06	1389.09	103.03	0.15	58	58	13	1%	s	577
Fuego	6.2	1286.06	1388.96	102.90	0.09	34	34	8	2%		523
Fuego	6.3	-	-			19	n.r.	7	5%	s, c	
Fuego	6.6	-	-			20	15	6	4%	s, c	
Fuego	7.1	-	-			21	n.r.	5	1%		
Fuego	7.2	-	-			35	n.r.	8	1%		
Fuego	7.6	-	-			21	19	6	2%	s	
Fuego	7.7	-	-			33	32	8	2%	s	
Fuego	7.4	-	-			56	56	12	1%	c	
Fuego	7.3	-	-			27	23	8	3%	s	
Fuego	8.1	-	-			11	n.r.	3	2%	s	
Fuego	8.2	-	-			24	n.r.	5	1%	s, c	
Fuego	8.3	-	-			72	68	18	2%		
Fuego	8.4	-	-			n.r.	n.r.	n.r.	n.r.	c	
Fuego	9.1	-	-			n.r.	n.r.	n.r.	n.r.	s, c	
Fuego	9.2*	1284.58	1387.55	102.97	0.12	98	82	26	2%	s	1063
Fuego	10.1	-	-			79	65	19	2%	s, c	
Fuego	10.2	-	-			n.r.	n.r.	n.r.	n.r.	s, c	
Fuego	11.1*	1283.92	1386.96	103.04	0.15	105	86	29	3%	s, c	1616
Fuego	11.2	-	-			10	7	3	4%	c	
Fuego	12.1	-	-			n.r.	n.r.	n.r.	n.r.	s, c	
Fuego	12.2	-	-			n.r.	n.r.	n.r.	n.r.	c	
Fuego	12.3*	d	d			132	112	38	3%	s, c	
Fuego	13.1	-	-			57	52	16	3%		
Fuego	13.2	-	-			13	11	3	2%	s	
Fuego	14.1	1285.09	1388.07	102.98	0.13	52	41	15	3%	s	1558
Fuego	15.1*	d	d			144	139	37	2%		

Fuego	19.1*	1283.91	1387.00	103.09	0.17	63	52	18	3%	s	1871
Fuego	19.2	-	-			32	31	11	4%	s, c	
Fuego	10.3a	1285.14	1388.23	103.09	0.17	11	10	3	2%	s	1547
Fuego	10.3b	1285.14	1387.98	102.84	0.07	19	17	6	4%	s	1125
Fuego	10.3c	-	-			n.r.	n.r.			s, c	

[a] Samples for which the volatile content of the glass has been analyzed are indicated with an asterisk (*).

[b] Fermi diad peak positions determined by peak fitting of Raman spectra collected from MI (see methods) at Virginia Tech. Values mark that CO_2 was not detected ; values marked as "d" indicate that CO_2 was detected, but the quality of the Raman spectra did not allow th and thus CO_2 density to be quantified (see text).

[c] values marked as "low" indicate that the density could not be quantified with the Fall et al. (2011) equation for the measured peak sep

[d] dimensions listed as "n.r." indicate dimensions that were not recorded. Where only one MI dimension is reported, the volume percen treating the MI as a sphere; in these cases, reconstructed CO_2 concentrations were not calculated.

[e] MI contain a chromite spinel (?)("s") or carbonates ("c") in addition to a bubble as indicated (see text).

[f] The minimum amount of CO_2 in the MI. This is calculated by Raman analysis of the bubble and by using a value of 0 ppm for the CO_2 c glass.

Table 4: Petrographic and Raman data for MI from Seguam.

Sample	MI Number[a]	Peak 1, cm^{-1} [b]	Peak 2, cm^{-1} [b]	Δ, cm^{-1}	CO$_2$ density, g/cm^3 [c]	long diameter MI, µm[d]	short diameter MI, µm[d]	Bubble diameter, µm[d]	Volume percent bubble[d]	daughter minerals[e]	CO$_2$ min[e]
Seguam	2.1*	1285.60	1388.26	102.67	0.01	106	93	27	2%		55
Seguam	3.1	-	-			22	20	5	2%	b	
Seguam	3.2	-	-			15	13	4	2%	b	
Seguam	4.1	-	-			17	16	6	6%	b	
Seguam	4.2	-	-			21	15	6	5%	c, b	
Seguam	5.1	d	d			73	64	20	3%		
Seguam	5.2*	1285.39	1388.12	102.73	0.03	135	117	38	3%		303
Seguam	5.3	-	-			18	14	5	3%		
Seguam	6.1*	1285.34	1388.11	102.77	0.04	159	166	37	1%		177
Seguam	7.1	-	-			176	127	36	2%	c, b	
Seguam	7.2	-	-			11	9	3	5%		
Seguam	7.3	-	-			28	22	7	3%		
Seguam	7.4	-	-			28	26	8	3%		
Seguam	7.5*	1285.31	1388.00	102.69	0.02	114	84	31	4%		223
Seguam	8.1	d	d			17	17	5	3%		
Seguam	8.2	d	d			43	40	12	3%		
Seguam	8.3*	1285.31	1388.00	102.69	0.01	138	136	41	3%		137
Seguam	8.4	-	-			68	62	19	3%		
Seguam	9.1*	d	d			88	82	29	4%	b	
Seguam	10.1*	1285.64	1388.34	102.70	0.02	82	66	20	2%		166
Seguam	10.2	-	-			28	25	7	2%	b	
Seguam	10.3	-	-			37	17	8	5%		
Seguam	11.1	d	d			23	21	8	5%		
Seguam	11.2	-	-			9	8	3	4%		
Seguam	11.3	-	-			15	15	5	3%		
Seguam	11.4	-	-			9	9	3	4%		
Seguam	12.1	d	d			100	94	24	2%		
Seguam	13.1*	1285.43	1388.19	102.77	0.04	88	87	28	3%		547
Seguam	14.1	-	-			89	75	24	3%		

Seguam	15.1*	1285.49	1388.32	102.83	0.07	82	59	20	3%		707
Seguam	16.1*	1285.47	1388.16	102.69	0.01	126	105	34	3%		144
Seguam	18.1	1285.45	1388.15	102.70	0.02	31	28	9	3%	b	245
Seguam	19.1	-	-			61	55	11	1%		
Seguam	20*	-	-			122	93	22	1%		
Seguam	22.1*	1285.18	1387.97	102.80	0.05	69	61	21	3%		672
Seguam	23.1*	1285.32	1388.01	102.69	0.01	117	93	28	2%		121
Seguam	23.2	-	-			35	31	10	3%		
Seguam	23.3	-	-			15	12	4	3%	c	
Seguam	24.1	-	-			15	14	3	1%		
Seguam	24.2	-	-			28	19	8	5%		
Seguam	24.3	-	-			n.r.	n.r.	n.r.	n.r.		
Seguam	24.4	-	-			23	17	6	3%		
Seguam	24.5	-	-			16	12	4	3%		
Seguam	24.6	-	-			30	22	7	3%		
Seguam	24.7	-	-			8	7	2	3%		
Seguam	24.8	-	-			26	21	7	3%		
Seguam	24.9*	1285.68	1388.38	102.69	0.02	80	49	8	0%		14
Seguam	24.10	-	-			49	42	13	3%		

[a] Samples for which the volatile content of the glass has been analyzed are indicated with an asterisk (*).

[a] Fermi diad peak positions determined by peak fitting of Raman spectra collected from MI (see methods) at Virginia Tech. Values markec that CO_2 was not detected ; values marked as "d" indicate that CO_2 was detected, but the quality of the Raman spectra did not allow the thus CO_2 density to be quantified (see text).

[b] values marked as "low" indicate that the density could not be quantified with the Fall et al. (2011) equation for the measured peak sepa

[c] dimensions listed as "n.r." indicate dimensions that were not recorded.

[d] MI indicated with a "s" contain a chromite spinel (?) in addition to a bubble. MI indicated with a "b" or "c" indicate that carbonates were bubble-glass interface. "b" indicates that bright carbonate minerals were visible in reflected light, and "c" indicates that carbonate was d spectroscopy (see text).

[e] The minimum amount of CO_2 in the MI calculated by Raman analysis of the bubble and by using a value of 0 ppm for the CO_2 contained

Table 5: Reconstructed CO_2 concentrations of MI and calculated trapping pressures

Sample	Number[a]	H_2O, wt%	CO_2 (glass), ppm[b]	P (glass), kbar[c]	Depth (glass), km[d]	% of CO_2 in bubble[e]	Estimated percent of total CO_2 contained in the bubble[f]	CO_2 (glass + bubble), ppm[g]	Error, ppm[h]		P (glass + bubble), kbar[c]	depth (glass + bubble), km[d]	CO_2 (glass + ideal gas), ppm[i]
Fuego	5.3*	4.03	189	1.9	7	63%	30%	513	+ 46	- 164	2.6	9	1110
Fuego	9.2	4.36	501	2.8	10	70%	60%	1684	+ 192	- 560	4.8	18	3093
Fuego	11.1*	4.29	511	2.7	10	78%	70%	2334	+ 288	- 871	5.8	21	3857
Fuego	19.1	4.11	488	2.6	9	81%	73%	2598	+ 287	- 1054	6.0	22	3773
Seguam	2.1	3.91	100	1.6	6	35%	10%	159	+ 10	- 25	1.8	6	536
Seguam	5.2	3.79	191	1.8	6	61%	38%	508	+ 57	- 122	2.4	9	1303
Seguam	6.1	3.90	114	1.7	6	62%	42%	299	+ 30	- 70	2.1	7	369
Seguam	7.5	3.69	179	1.7	6	55%	31%	407	+ 36	- 118	2.2	8	1518
Seguam	8.3	4.00	181	1.9	7	46%	21%	344	+ 28	- 66	2.2	8	1271
Seguam	10.1	3.87	502	2.5	9	24%	25%	656	+ 36	- 79	2.8	10	2708
Seguam	13.1	4.50	200	2.3	8	79%	52%	802	+ 94	- 282	3.4	13	1769
Seguam	15.1	3.81	48	1.5	5	93%	59%	756	+ 107	- 397	2.9	11	316
Seguam	16.1	4.02	202	1.9	7	29%	22%	293	+ 13	- 41	2.1	8	855
Seguam	22.1	4.19	224	2.1	8	75%	57%	896	+ 102	- 305	3.4	12	1708
Seguam	23.1	3.90	197	1.8	7	38%	19%	322	+ 20	- 60	2.1	8	1089
Seguam	24.9	2.92	55	1.0	3	18%	3%	77	+ 1	- 9	1.0	4	80
Kil Iki Nar R	3w	0.30	78	0.2	1	48%	20%	151	+ 35	- 34	0.3	1	734
Kil Iki Nar R	4w	0.19	230	0.5	2	63%	51%	624	+ 116	- 183	1.3	5	3883
Kap 8 Nat R	1w	0.96	140	0.4	1	89%	80%	1318	+ 239	- 599	2.7	10	1528
Kap 8 Nat R	3w	0.63	152	0.4	1	80%	66%	744	+ 239	- 281	1.6	6	2435
Kap 8 Nat R	6w	0.48	342	0.7	3	61%	64%	873	+ 108	- 325	1.8	7	2741
Kap 8 Nat R	7w	0.55	233	0.5	2	88%	85%	1944	+ 362	- 825	3.7	13	4969

[a] Samples indicated with an asterisk contain carbonates (see text, Table 2).

[b] Values have not been reconstructed to include CO_2 lost to the bubble.

[c] Pressures were calculated using VolatileCalc (Newman & Lowenstern, 2002)

[d] Depths were calculated using a 3.5 km/kbar gradient

[e] Percent of CO_2 in the bubble is calculated using the mass balance approach described by Esposito et al. (2011) (see text and appendix).

[f] Percentage of total CO_2 in the MI contained in the bubble estimated using Raman analysis of the bubble and typical CO_2 contents of MI glass from the literature (Anderson & Brown, 1993; Zimmer et al., 2010; Lloyd et al., 2013) (see figure 7).

[g] CO_2 concentrations were reconstructed to include CO_2 contained in the bubble measured *in situ* by Raman spectroscopy (see text)

[h] Asymetrical error values are produced by propogating uncertainty through the mass balance calculations. See appendix for a discussion of error treatment.

[i] CO_2 concentrations reconstructed using the Ideal Gas Law (see text).